

THE STELLAR POPULATION HISTORIES OF EARLY-TYPE GALAXIES. II. CONTROLLING PARAMETERS OF THE STELLAR POPULATIONS

S. C. TRAGER^{1,2}

The Observatories of the Carnegie Institution of Washington, 813 Santa Barbara St., Pasadena, CA 91101; sctrager@ociw.edu

S. M. FABER

UCO/Lick Observatory and Board of Studies in Astronomy and Astrophysics, University of California, Santa Cruz, Santa Cruz, CA 95064; faber@ucolick.org

GUY WORTHEY

Department of Physics and Astronomy, St. Ambrose University, Davenport, IA 52803-2829; gworthy@saunix.sau.edu

J. JESÚS GONZÁLEZ

Instituto de Astronomía—UNAM, Apdo Postal 70-264, México D.F., Mexico; jesus@astroscu.unam.mx

Accepted for publication in the Astronomical Journal

ABSTRACT

This paper analyzes single-stellar-population (SSP) equivalent parameters for 50 local elliptical galaxies as a function of their structural parameters. The galaxy sample is drawn from the high-quality spectroscopic surveys of González (1993) and Kuntschner (1999). The basic data are central values of SSP-equivalent ages, t , metallicities, $[Z/H]$, and “enhancement” ratios, $[E/Fe]$, derived in Paper I, together with global structural parameters including velocity dispersions, radii, surface brightnesses, masses, and luminosities.

The galaxies fill a two-dimensional plane in the four-dimensional space of $[Z/H]$, $\log t$, $\log \sigma$, and $[E/Fe]$. SSP age, t and velocity dispersion, σ , can be taken as the two independent parameters that specify a galaxy’s location in this “hyperplane.” The hyperplane can be decomposed into two sub-relations: (1) a “Z-plane,” in which $[Z/H]$ is a linear function of $\log \sigma$ and $\log t$; and (2) a relation between $[E/Fe]$ and σ in which $[E/Fe]$ is larger in high- σ galaxies. Velocity dispersion is the only structural parameter that is found to modulate the stellar populations; adding other structural variables such as I_e or r_e does not predict $[Z/H]$ or $[E/Fe]$ more accurately.

Cluster and field ellipticals follow the same hyperplane, but their (σ, t) distributions within it differ. Most Fornax and Virgo cluster galaxies are old, with a only a small sprinkling of galaxies to younger ages. The field ellipticals span a larger range in SSP age, with a tendency for lower- σ galaxies to be younger. The present sample thus suggests that the distribution of local ellipticals in the (σ, t) plane may depend on environment. Since the (σ, t) distribution affects all two-dimensional projections involving SSP parameters, many of the familiar scaling laws attributed to ellipticals may also depend on environment. Some evidence for this is seen in the current sample. For example, only Fornax ellipticals show the classic mass-metallicity relation, whereas other sub-samples do not.

The tight Mg- σ relations of these ellipticals can be understood as two-dimensional projections of the metallicity hyperplane showing it edge on. At fixed σ , young age tends to be offset by high $[Z/H]$, preserving Mg nearly constant. The tightness of the Mg- σ relations does not necessarily imply a narrow range of ages at fixed σ .

Although SSP parameters are heavily weighted by young stars, modeling them still places tight constraints on the total star formation history of elliptical galaxies. The relation between $[E/Fe]$ and σ is consistent with a higher effective yield of Type II SNe elements at higher σ . This might occur if the IMF is enhanced in massive stars at high σ , or if more SNe II-enriched gas is retained by deeper galactic potential wells. Either way, modulating Type II yields vs. σ seems to fit the data better than modulating Type Ia yields.

The Z-plane is harder to explain and may be a powerful clue to star formation in elliptical galaxies if it proves to be general. Present data favor a “frosting” model in which low apparent SSP ages are produced by adding a small frosting of younger stars to an older “base” population (assuming no change in σ). If the frosting abundances are close to or slightly greater than the base population, simple two-component models run along lines of constant σ in the Z-plane, as required. This favors star formation from well-mixed pre-enriched gas rather than unmixed low-metallicity gas from an accreted object.

Subject headings: galaxies: elliptical and lenticular, cD — galaxies: stellar content — galaxies: abundances — galaxies: formation — galaxies: evolution

1. INTRODUCTION

The star formation histories of elliptical galaxies, once thought to be very simple—old and metal-rich (Baade 1963)—have come under increasing scrutiny in the last three decades (e.g., Spinrad & Taylor 1971; Faber 1973, 1977; O’Connell 1976, 1980; Pickles 1985; Peletier 1989; Schweizer & Seitzer

1992; González 1993; Worthey 1994; Lee 1994; Renzini 1995, 1998; Tantaló, Chiosi & Bressan 1998a; Kuntschner 1998; Jørgensen 1999). Currently there are two basic models for elliptical galaxy formation: hierarchical clustering of small objects into larger galaxy-sized units with accompanying star formation over time (e.g., Blumenthal et al. 1984; Kauffmann, White & Guiderdoni 1993), versus monolithic collapse and star forma-

¹Carnegie Starr Fellow

²Hubble Fellow

tion in a nearly coeval single early burst (e.g., Eggen, Lynden-Bell & Sandage 1962; Larson 1974; Arimoto & Yoshii 1987). Measurements of the spectral energy distributions (SEDs) and spectral features of elliptical galaxies can provide a test of these scenarios. For example, evidence for substantial intermediate-age stellar populations (between 1 and 10 Gyr) might favor hierarchical models, which more naturally have extended star formation over time. A goal of the present series is to assess the evidence for such intermediate-age populations.

The first paper of this series (Trager et al. 2000, hereafter Paper I) used Lick absorption-line strengths for a sample of local elliptical galaxies observed by González (1993, hereafter G93) to derive single-stellar-population (SSP) equivalent parameters t (age), $[Z/H]$ (metallicity), and $[E/Fe]$ (“enhancement ratio,” see below). Single-burst model line-strengths by Worthey (1994, hereafter W94) were corrected for the effect of non-solar abundance ratios using theoretical spectral calculations by Tripicco & Bell (1995, hereafter TB95). The resultant SSP ages cover a range of 1 to 18 Gyr (including observational errors), while the ranges in $[Z/H]$ and $[E/Fe]$ are fairly narrow. These parameters, particularly the ages, are based on the assumption that $H\beta$ faithfully traces the mean temperature of the main-sequence turnoff and is not seriously affected by other hot stellar populations. Evidence supporting this assumption was presented in Paper I.

In deriving single-burst SSP parameters for elliptical galaxies, we do not mean to imply that their star formation histories were actually single bursts. In fact, our favored “frosting” model (Section 7) involves adding a minority of young stars to an older base population. Our use of SSP parameters is simply a convenient way of condensing all the presently measured line strength data into just three numbers: light-weighted age, $[Z/H]$, and $[E/Fe]$. For the moment, that is all the observations allow. It is our hope that SSP parameters will be adopted by those who model the full evolutionary history of elliptical galaxies (e.g., Arimoto & Yoshii 1987; Vazdekis et al. 1996; Tantalo et al. 1998b) and that they will serve as a convenient meeting ground between models and data. We show below that, even though SSP parameters are heavily influenced by the light of any young stars that may be present, modeling them still places important constraints on the total history of star formation in ellipticals.

This paper explores the central stellar populations of a sample of local elliptical galaxies and develops correlations among them and with parent-galaxy structural parameters. Many previous works have studied such correlations, but most have focused on *raw* line strengths. Only three other studies, to our knowledge, have measured ages (using Balmer lines) and developed correlations based on underlying stellar populations. Tantalo, Chiosi & Bressan (1998) studied the G93 galaxies using models based on the “Padua” isochrones. Their correction for non-solar abundance ratios was approximate, however, leading to systematic errors in derived age, $[Z/H]$, and $[E/Fe]$ (Paper I). Kuntschner (1999) studied ellipticals in Fornax using high-quality data, which we add to our sample here. He found that Fornax ellipticals were mainly old, and also discovered a strong relation between $[E/Fe]$ and σ , which we confirm. Jørgensen (1999) studied Coma ellipticals using line-strength models by Vazdekis et al. (1996). Her conclusions foreshadow ours in many respects, but some seem in retrospect to be the product of observational errors. All three of these papers are discussed in Section 3.6.

The outline of this paper is as follows. A brief review of

the G93 and Kuntschner (1999) samples, line-strength data, SSP-equivalent stellar population parameters, and structural parameters is given in Section 2. Section 3 presents the sample distribution in the four-dimensional space spanned by $[Z/H]$, $\log t$, $\log \sigma$, and $[E/Fe]$; this proves to be a highly flattened, two-dimensional “hyperplane” that in turn consists of two sub-relations, a “Z-plane,” plus a linear $[E/Fe]$ - σ relation. Section 4 shows how projections of this hyperplane depend on the distribution of points within it, and thus how the appearance of two-dimensional scaling laws can vary depending on this distribution. Section 5 illustrates these effects using two classic scaling laws—the mass-metallicity relation and the Mg - σ relation. Possible evidence for environmental variation in the former is presented. Sections 6 and 7 investigate the origins of the hyperplane. The Z-plane in particular appears difficult to explain and, if it proves general, will place very tight constraints on the history of star formation in local elliptical galaxies. Section 8 summarizes our findings and conclusions.

2. DATA AND DERIVED PARAMETERS

This section briefly describes the G93 and Fornax samples, the Lick/IDS line-strength system, the models used to transform line strengths into SSP-equivalent parameters, and final population parameters for the central ($r_e/8$) aperture observations of G93 and Fornax ellipticals. A complete description of the data and their transformation into stellar population parameters was given in Paper I. Structural parameters drawn from the literature for these galaxies are also given.

2.1. Sample

Trager (1997) showed that deriving SSP parameters from Balmer and metal lines requires line-strength data of very high quality, with errors preferably $< 0.1\text{\AA}$. Only three published samples approach this level of accuracy: González (1993), Kuntschner (1998), and Fisher, Franx, and Illingworth (1995). The original G93 sample consists of 41 early-type galaxies, of which 40 are included in the present study (NGC 4278 is discarded because of its strong emission). All G93 galaxies used here have been classified as elliptical (or compact elliptical) in the RC3 (de Vaucouleurs et al. 1991) or the RSA (Sandage & Tammann 1987) and Carnegie Atlas (Sandage & Bedke 1994), except for NGC 507 and NGC 6703, both classified as SA0 in the RC3 but not included in the RSA or Carnegie Atlas, and NGC 224, the bulge of the Sb galaxy Messier 31.

The environmental distribution of the G93 sample is skewed toward relatively low-density environments. As discussed in Paper I, most of the galaxies are in small groups of varying richness, many are relatively isolated, and six are members of the Virgo Cluster. Only one is in a rich cluster (NGC 547 in Abell 194). Environmental effects on the stellar populations of ellipticals are discussed in Sections 4 and 5 below.

The G93 sample is augmented here with data from Kuntschner (1999, hereafter K98; cf. Kuntschner & Davies 1998) on early-type galaxies in the Fornax cluster. These data have been carefully transformed to the Lick line-strength system. Eleven of the 22 galaxies in K98 are ellipticals. SSP parameters have been derived for them following the method below, after correcting the central line strengths (Table 3.4 of K98) to the $r_e/8$ aperture using the gradients presented in Table 7.2 of K98.

The high-accuracy elliptical galaxy sub-sample of Fisher et al. (1995) repeats galaxies in G93 and agrees well with it. These data have therefore not been used here.

2.2. Ages, metallicities, and enhancement ratios

Paper I describes our technique for inverting line strengths to determine SSP parameters. Ages, metallicities, and enhancement ratios of old stellar populations are determined by comparing observed absorption-line strengths to the *single-burst stellar population (SSP)* models of W94, which depend on metallicity and age. The line-strengths of the Worthey models correspond to solar abundance ratios; these have been corrected for non-solar abundance ratios as described in Paper I using the theoretical spectral calculations of TB95, who tabulated the response of the Lick/IDS indices to changes in the abundance ratios of important elements. SSP-equivalent t , $[Z/H]$, and $[E/Fe]$ are derived for each galaxy by searching a finely-spaced grid of points in $(H\beta, Mg b, \langle Fe \rangle)$ space. Central line strengths corrected to the $r_e/8$ aperture are presented in Figure 1 for the G93 and K98 samples.

Table 1 presents derived SSP parameters (t , $[Z/H]$, $[E/Fe]$) and their uncertainties through the $r_e/8$ aperture under the preferred enrichment model 4 of Paper I. The quantity $[E/Fe]$ is similar to the quantity $[\alpha/Fe]$ used by other authors, but we have fine-tuned the elements in the “E” group based on current knowledge. The E group in model 4 contains Ne, Na, Mg, Si, S, as well as C and O; the abundance of these elements is slightly enhanced relative to the mean. A “depressed group” contains the Fe-peak elements, while all other elements are held constant (at fixed $[Z/H]$). See Paper I for further details on element grouping and notation.

The above grouping of elements is based partly on observed elliptical line-strengths and partly on current nucleosynthetic theory. The observed strength of Mg (and Na) in ellipticals strongly implies the enhancement of O and other α -elements, as these elements are nucleosynthetically linked (Woosley & Weaver 1995). (Note that the nominal α -element Ca seems to belong with the Fe-peak elements in ellipticals based on its line strengths [Worthey 1998; Trager et al. 1998]; this anomaly is unexplained.) The element C is also clearly strong in giant ellipticals and is placed in the E group for that reason (Worthey 1998; Paper I). On the other hand, the weak Fe lines of ellipticals suggest a reduction in Fe-peak elements (Worthey 1998). All remaining elements have been left unchanged for lack of information, although in retrospect N should probably have been grouped in the E group, but this makes little difference to the final results (see Paper I).

Paper I argued that it is actually incorrect to think of the E elements as being enhanced in elliptical galaxies; since they dominate $[Z/H]$ by mass, their abundance essentially *is* $[Z/H]$. If $[E/Fe]$ is > 0 , it must rather be that the Fe-peak elements are *depressed* (relative to the average element). The Fe-peak elements contribute so little to the overall metallicity (only 8% at solar abundance) that changing their abundance by large amounts does not significantly affect either $[E/H]$ or $[Z/H]$. Thus, in what follows we think consistently of the relative depression of the Fe-peak elements rather than the relative enhancement of the E elements. Specifically, if $[E/Fe] \neq 0$, then $[E/Z]$ is very slightly positive while $[Fe/Z]$ is nearly equal to $-[E/Fe]$.

Table 1 also presents the further quantities $[Fe/H]$ and $[E/H]$. These are computed using the equations

$$[Fe/H] = [Z/H] - A[E/Fe] \quad (1)$$

and

$$[E/H] = [Z/H] + (1 - A)[E/Fe], \quad (2)$$

where $A = 0.929$ for enrichment model 4 (see Paper I for details).

2.3. Global parameters

Structural parameters are presented in Tables 2a and 2b. Table 2a gives distance-independent quantities: velocity dispersions (from G93 and K98), B_T^O magnitudes (Section 2.4), mean ellipticities and effective radii in arc seconds (collected from the literature and homogenized by G93), mean effective surface brightnesses, isophotal shape parameters a_4/a , rotation parameters $(v/\sigma_0)^*$, morphological disturbance parameters Σ_{SS} (Schweizer et al. 1990, Schweizer & Seitzer 1992), nuclear profile shapes (power-law or core; Faber et al. 1997), and presence and type of AGN activity, if any. Table 2b presents distance-dependent quantities: redshifts (repeated from Table 1 of Paper I), distance moduli from SBF measurements (Tonry et al., in prep.) or flow-corrected distances from Tonry et al. (priv. comm.), absolute magnitudes using SBF distances, effective radii in parsecs, mean effective surface brightnesses in solar units (not distance-dependent but needed in the computation of mass-to-light ratios), galaxy masses in solar masses, and mass-to-(blue)-light ratios in solar units. Many of these quantities will be used in future papers. Details and references are given in the footnotes to the tables.

2.4. Magnitudes and colors

Table 3 presents B_T^O , $(U - V)$, and $(B - V)$ in various apertures for all galaxies except NGC 7052, for which no published global photometry was found. These values are corrected for Galactic absorption and redshift (but not internal extinction) following the precepts of the RC3. “Total” and “effective” colors are drawn from the RC3, Poulain (1988), or Poulain & Nieto (1994) as appropriate. A “central” color through $r_e/8$ is computed by taking effective colors and correcting them inward using the average color gradients of early-type galaxies from Peletier et al. (1990) and Goudfrooij et al. (1994). The mean $(B - V)$ color gradient is taken from Goudfrooij et al. (1994):

$$\frac{\Delta(B - V)}{\Delta(\log r)} = -0.06 \pm 0.01 \text{ mag/dex} \quad (3)$$

(using 53 galaxies). The mean $(U - B)$ gradient is from Peletier et al. (1990):

$$\frac{\Delta(U - B)}{\Delta(\log r)} = -0.11 \pm 0.03 \text{ mag/dex}, \quad (4)$$

for a mean $(U - V)$ gradient of

$$\frac{\Delta(U - V)}{\Delta(\log r)} = -0.17 \pm 0.03 \text{ mag/dex}. \quad (5)$$

This is consistent with estimates by Peletier, Valentijn & Jameson (1990) and the combined results of Franx, Illingworth & Heckman (1989) and Goudfrooij et al. (1994). The $r_e/8$ colors are then computed as

$$(U - V)_{r_e/8}^O = (U - V)_e^O + 0.15 \quad (6)$$

and

$$(B - V)_{r_e/8}^O = (B - V)_e^O + 0.05. \quad (7)$$

TABLE 1
CENTRAL AGES, METALLICITIES AND ENHANCEMENT RATIOS THROUGH $r_e/8$ APERTURE (ENRICHMENT MODEL 4)

Name	Age (Gyr)	[Z/H]	[E/Fe]	[Fe/H]	[E/H]
G93 ellipticals:					
NGC 221	3.0 ± 0.7	0.00 ± 0.05	-0.08 ± 0.01	0.07 ± 0.05	-0.01 ± 0.05
NGC 224	6.0 ± 1.6	0.39 ± 0.05	0.19 ± 0.02	0.21 ± 0.05	0.40 ± 0.05
NGC 315	5.4 ± 1.5	0.34 ± 0.06	0.25 ± 0.02	0.11 ± 0.06	0.36 ± 0.06
NGC 507	7.4 ± 2.8	0.19 ± 0.07	0.20 ± 0.03	0.00 ± 0.08	0.20 ± 0.07
NGC 547	8.9 ± 2.4	0.24 ± 0.05	0.26 ± 0.02	-0.00 ± 0.05	0.26 ± 0.05
NGC 584	2.5 ± 0.3	0.49 ± 0.03	0.22 ± 0.01	0.29 ± 0.03	0.51 ± 0.03
NGC 636	4.1 ± 0.7	0.34 ± 0.07	0.11 ± 0.02	0.24 ± 0.07	0.35 ± 0.07
NGC 720	4.5 ± 2.3	0.46 ± 0.17	0.33 ± 0.04	0.15 ± 0.17	0.48 ± 0.17
NGC 821	7.5 ± 1.2	0.23 ± 0.03	0.15 ± 0.01	0.09 ± 0.03	0.24 ± 0.03
NGC 1453	7.6 ± 1.9	0.32 ± 0.06	0.22 ± 0.02	0.12 ± 0.06	0.34 ± 0.06
NGC 1600	8.1 ± 2.2	0.37 ± 0.06	0.23 ± 0.02	0.16 ± 0.06	0.39 ± 0.06
NGC 1700	2.3 ± 0.3	0.50 ± 0.03	0.16 ± 0.01	0.35 ± 0.03	0.51 ± 0.03
NGC 2300	5.9 ± 1.5	0.38 ± 0.05	0.25 ± 0.02	0.15 ± 0.05	0.40 ± 0.05
NGC 2778	5.4 ± 1.8	0.30 ± 0.09	0.23 ± 0.03	0.09 ± 0.09	0.32 ± 0.09
NGC 3377	3.7 ± 0.8	0.20 ± 0.06	0.20 ± 0.02	0.01 ± 0.06	0.21 ± 0.06
NGC 3379	8.6 ± 1.4	0.22 ± 0.03	0.21 ± 0.01	0.02 ± 0.03	0.23 ± 0.03
NGC 3608	6.9 ± 1.5	0.26 ± 0.05	0.17 ± 0.02	0.10 ± 0.05	0.27 ± 0.05
NGC 3818	5.6 ± 1.8	0.37 ± 0.08	0.23 ± 0.03	0.16 ± 0.08	0.39 ± 0.08
NGC 4261	15.5 ± 3.3	0.19 ± 0.04	0.20 ± 0.01	0.00 ± 0.04	0.20 ± 0.04
NGC 4374	12.2 ± 2.2	0.13 ± 0.03	0.21 ± 0.01	-0.07 ± 0.03	0.14 ± 0.03
NGC 4472	7.9 ± 1.7	0.26 ± 0.05	0.21 ± 0.02	0.06 ± 0.05	0.27 ± 0.05
NGC 4478	4.6 ± 2.3	0.30 ± 0.10	0.15 ± 0.03	0.16 ± 0.10	0.31 ± 0.10
NGC 4489	2.5 ± 0.4	0.14 ± 0.06	0.03 ± 0.02	0.11 ± 0.06	0.14 ± 0.06
NGC 4552	10.5 ± 1.2	0.28 ± 0.04	0.23 ± 0.01	0.07 ± 0.04	0.30 ± 0.04
NGC 4649	11.7 ± 1.5	0.29 ± 0.04	0.25 ± 0.01	0.06 ± 0.04	0.31 ± 0.04
NGC 4697	8.9 ± 1.9	0.06 ± 0.06	0.10 ± 0.02	-0.03 ± 0.06	0.07 ± 0.06
NGC 5638	8.3 ± 1.4	0.20 ± 0.03	0.19 ± 0.01	0.02 ± 0.03	0.21 ± 0.03
NGC 5812	5.3 ± 1.1	0.39 ± 0.04	0.20 ± 0.01	0.20 ± 0.04	0.40 ± 0.04
NGC 5813	18.3 ± 2.3	-0.03 ± 0.03	0.21 ± 0.01	-0.23 ± 0.03	-0.02 ± 0.03
NGC 5831	2.6 ± 0.3	0.54 ± 0.03	0.19 ± 0.01	0.36 ± 0.03	0.55 ± 0.03
NGC 5846	13.5 ± 3.3	0.15 ± 0.05	0.22 ± 0.02	-0.05 ± 0.05	0.17 ± 0.05
NGC 6127	11.6 ± 2.2	0.18 ± 0.04	0.23 ± 0.02	-0.03 ± 0.04	0.20 ± 0.04
NGC 6702	1.5 ± 0.1	0.70 ± 0.07	0.15 ± 0.03	0.56 ± 0.08	0.71 ± 0.07
NGC 6703	4.3 ± 0.7	0.32 ± 0.06	0.15 ± 0.02	0.18 ± 0.06	0.33 ± 0.06
NGC 7052	12.5 ± 3.1	0.17 ± 0.05	0.24 ± 0.02	-0.05 ± 0.05	0.19 ± 0.05
NGC 7454	5.0 ± 1.0	-0.06 ± 0.04	0.06 ± 0.02	-0.12 ± 0.04	-0.06 ± 0.04
NGC 7562	7.6 ± 1.6	0.21 ± 0.04	0.17 ± 0.01	0.05 ± 0.04	0.22 ± 0.04
NGC 7619	14.4 ± 2.2	0.21 ± 0.03	0.18 ± 0.01	0.04 ± 0.03	0.22 ± 0.03
NGC 7626	12.8 ± 2.4	0.17 ± 0.03	0.25 ± 0.01	-0.06 ± 0.03	0.19 ± 0.03
NGC 7785	8.4 ± 2.3	0.21 ± 0.05	0.16 ± 0.02	0.06 ± 0.05	0.22 ± 0.05
Fornax cluster ellipticals:					
NGC 1336	15.9 ± 3.0	-0.32 ± 0.04	0.13 ± 0.04	-0.44 ± 0.05	-0.31 ± 0.04
NGC 1339	12.7 ± 4.8	0.12 ± 0.07	0.22 ± 0.03	-0.08 ± 0.08	0.14 ± 0.07
NGC 1351	17.0 ± 3.3	-0.10 ± 0.05	0.16 ± 0.03	-0.25 ± 0.06	-0.09 ± 0.05
NGC 1373	6.3 ± 2.0	0.13 ± 0.08	0.13 ± 0.03	0.01 ± 0.08	0.14 ± 0.08
NGC 1374	9.5 ± 2.6	0.13 ± 0.07	0.18 ± 0.02	-0.04 ± 0.07	0.14 ± 0.07
NGC 1379	10.9 ± 2.9	-0.08 ± 0.06	0.16 ± 0.03	-0.23 ± 0.07	-0.07 ± 0.06
NGC 1399	11.5 ± 2.4	0.29 ± 0.06	0.25 ± 0.03	0.06 ± 0.07	0.31 ± 0.06
NGC 1404	9.0 ± 2.5	0.25 ± 0.05	0.14 ± 0.03	0.12 ± 0.06	0.26 ± 0.05
NGC 1419	13.7 ± 3.2	-0.09 ± 0.06	0.09 ± 0.03	-0.17 ± 0.07	-0.08 ± 0.06
NGC 1427	12.2 ± 1.6	-0.07 ± 0.03	0.11 ± 0.02	-0.17 ± 0.04	-0.06 ± 0.03
IC 2006	16.9 ± 4.2	0.06 ± 0.06	0.16 ± 0.03	-0.09 ± 0.07	0.07 ± 0.06

TABLE 2A
DISTANCE-INDEPENDENT QUANTITIES

Name	σ (km s ⁻¹)	B_T^0	ϵ	r_e ($''$)	$\langle \mu_e \rangle$	a_4/a $\times 100$	$(v/\sigma_0)^*$	Σ_{SS}	Nuclear profile	AGN?
NGC 221	72 ± 3	8.72	0.23	39	18.70	0.00	0.89	...	\	no
NGC 224	156 ± 4	5.58	0.18	0.78	...	\	no
NGC 315	321 ± 4	11.87	0.27	55	22.26	-0.30	0.09	...	\	LINER
NGC 507	262 ± 6	12.13	0.12	77	23.06	...	0.09	no
NGC 547	236 ± 4	12.92	0.16	25	22.02	0.00	0.24
NGC 584	193 ± 3	11.21	0.30	30	20.58	1.50	1.55	2.78
NGC 636	160 ± 3	12.22	0.13	19	20.72	0.80	1.04	1.48
NGC 720	239 ± 5	11.13	0.39	40	21.16	0.35	0.32	...	\	...
NGC 821	189 ± 3	11.72	0.32	36	21.49	2.50	0.70	no
NGC 1336	96 ± 5	13.08	0.26	27	22.16
NGC 1339	158 ± 9	12.50	0.29	17	20.64	...	1.22
NGC 1351	157 ± 9	12.48	0.34	26	21.33	...	0.80
NGC 1373	75 ± 4	14.08	0.23	10	21.00
NGC 1374	185 ± 10	12.01	0.09	30	21.26
NGC 1379	130 ± 7	11.87	0.03	42	21.79
NGC 1399	375 ± 21	10.44	0.10	42	20.68	0.10	0.25	...	\	...
NGC 1404	260 ± 14	10.98	0.11	27	20.02
NGC 1419	117 ± 6	13.46	0.00	11	20.59
NGC 1427	175 ± 10	11.81	0.31	33	21.34	...	0.39
IC 2006	136 ± 8	12.25	0.10	29	21.45
NGC 1453	286 ± 4	12.26	0.17	28	21.47	-0.50	0.62	1.48
NGC 1600	315 ± 4	11.83	0.33	47	22.15	-0.75	0.03	...	\	...
NGC 1700	227 ± 3	12.01	0.27	24	20.82	0.70	0.59	3.70	\	...
NGC 2300	252 ± 3	11.77	0.16	34	21.42	0.60	0.08	2.85	...	no
NGC 2778	154 ± 3	13.21	0.21	19	21.60	-0.20	0.74
NGC 3377	108 ± 3	11.07	0.50	34	20.78	1.05	0.86	1.48	\	no
NGC 3379	203 ± 3	10.18	0.09	35	20.15	0.10	0.72	0.00	\	LINER?
NGC 3608	178 ± 3	11.69	0.19	35	21.40	-0.20	0.27	0.00	\	LINER:
NGC 3818	173 ± 4	12.47	0.39	21	21.17	2.30	0.93	1.30
NGC 4261	288 ± 3	11.36	0.21	39	21.26	-1.30	0.10	1.00	...	LINER
NGC 4374	282 ± 3	10.01	0.14	52	20.73	-0.40	0.09	2.30	...	LINER
NGC 4472	279 ± 4	9.33	0.16	104	21.40	-0.25	0.43	...	\	Sy2?
NGC 4478	128 ± 2	12.21	0.19	14	19.87	-0.75	0.84	...	\	no
NGC 4489	47 ± 4	12.88	0.12	32	22.23	-0.20	1.49
NGC 4552	252 ± 3	10.57	0.07	30	20.22	0.01	0.28	...	\	trans
NGC 4649	310 ± 3	9.70	0.17	74	21.11	-0.35	0.42	...	\	no
NGC 4697	162 ± 4	10.07	0.41	75	21.40	1.30	0.71	0.00	\	...
NGC 5638	154 ± 3	12.06	0.08	34	21.58	0.20	0.73	no
NGC 5812	200 ± 3	11.83	0.05	22	20.65	0.00	0.52
NGC 5813	205 ± 3	11.42	0.16	49	21.83	0.01	0.51	...	\	LINER:
NGC 5831	160 ± 3	12.31	0.17	27	21.44	0.50	0.19	3.60	...	no
NGC 5846	224 ± 4	10.91	0.07	83	22.26	0.00	0.10	0.30	...	trans:
NGC 6127	239 ± 4	12.92	0.06	22	21.60	...	0.11
NGC 6702	174 ± 3	13.04	0.23	29	22.16	-0.40	0.18	LINER?
NGC 6703	183 ± 3	11.97	0.02	24	20.88	0.00	0.30	LINER?
NGC 7052	274 ± 4	12.69	0.45	32	22.30	0.01	0.34
NGC 7454	106 ± 3	12.63	0.35	26	21.60	0.00	0.13
NGC 7562	248 ± 3	12.37	0.29	25	21.28	0.01	0.06
NGC 7619	300 ± 3	11.93	0.24	32	21.52	0.30	0.53	0.00	...	no
NGC 7626	253 ± 3	12.06	0.13	38	21.88	0.01	0.12	2.60	...	LINER?
NGC 7785	240 ± 3	12.41	0.42	27	21.46	-1.20	0.47

NOTE.— Col. (1): Galaxy name. Col. (2): Velocity dispersion within $r_e/8$ aperture from González (1993) or central velocity dispersion from Kuntschner (1998). Col. (3): Total spheroid B magnitude corrected for Galactic absorption and redshift; see Table 3 for details. Col. (4): Mean ellipticity from $\sim 7''$ to r_e , from González (1993) or Caon et al. (1994). Col. (5): Effective radius in arc seconds in the Seven Samurai \sqrt{ab} system from Faber et al. (1989), from González (1993), or from Caon et al. (1994). Col. (6): Mean effective surface brightness inside r_e in B magnitudes per square arc second, from Faber et al. (1989) or computed from values in Caon et al. (1994). Col. (7): Isophotal shape parameter, $a_4/a \times 100$, from Faber et al. (1997), Bender, Burstein & Faber (1992), and Bender (priv. comm.). Col. (8): Rotation parameter $(v/\sigma_0)^* = \langle v/\sigma_0 \rangle / \langle v/\sigma_0 \rangle_{\text{oblate}}$, where $\langle v/\sigma_0 \rangle_{\text{oblate}} = [\epsilon/(1-\epsilon)]^{1/2}$, as defined in Bender (1988). Taken from Faber et al. (1997) and Bender, Burstein & Faber (1992), or derived from data in González (1993) and Kuntschner (1998) when necessary. The rotational velocity for NGC 4489 is taken from Prugniel & Simien (1996), and its $(v/\sigma_0)^*$ should be considered an upper limit. NGC 1427 has a kinematically decoupled core (e.g., Kuntschner 1998); its value is an upper limit and may be much closer to zero. Col. (9): Morphological disturbance parameter from Schweizer & Seitzer (1992). Col. (10): Nuclear profile shape from Faber et al. (1997): “\” denotes core; “\” denotes power-law. Col. (11): AGN detection and classification from Ho, Filippenko & Sargent (1997): Sy=Seyfert; trans=intermediate AGN (LINER/H II nucleus); LINER=LINER; no=no AGN detected. “:” denotes uncertain classification, “?” denotes highly uncertain classification.

TABLE 2B
DISTANCE-DEPENDENT QUANTITIES

Name	cz (km s ⁻¹)	$(m-M)_{CMB}$	M_B	$\log r_e$ (pc)	$\log I_e$ (L_\odot pc ⁻²)	$\log M$ (M_\odot)	M/L_B (M_\odot/L_\odot)
NGC 221	-204 ± 7	24.63	-15.91	2.20	3.32	8.58	2.27
NGC 224	-300 ± 7	24.48
NGC 315	4942 ± 6	34.02	-22.15	4.23	1.90	11.91	11.26
NGC 507	4908 ± 11	33.87	-21.74	4.35	1.58	11.85	11.99
NGC 547	5468 ± 6	34.12	-21.20	3.91	1.99	11.32	10.25
NGC 584	1866 ± 6	31.60	-20.39	3.48	2.57	10.72	4.84
NGC 636	1860 ± 6	32.45	-20.23	3.45	2.51	10.53	4.04
NGC 720	1741 ± 11	32.29	-21.16	3.75	2.34	11.17	6.91
NGC 821	1730 ± 7	31.99	-20.27	3.64	2.20	10.86	7.47
NGC 1336	1439 ± 11	31.52	-18.44	3.42	1.94	10.05	5.92
NGC 1339	1355 ± 12	31.52	-19.02	3.22	2.54	10.28	6.28
NGC 1351	1529 ± 13	31.52	-19.04	3.40	2.27	10.46	7.65
NGC 1373	1341 ± 10	31.52	-17.44	2.99	2.40	9.41	3.35
NGC 1374	1349 ± 13	31.52	-19.51	3.47	2.30	10.67	8.63
NGC 1379	1360 ± 11	31.52	-19.65	3.61	2.08	10.51	4.96
NGC 1399	1431 ± 28	31.52	-21.08	3.61	2.53	11.43	14.85
NGC 1404	1923 ± 17	31.52	-20.54	3.42	2.79	10.92	6.04
NGC 1419	1574 ± 10	31.52	-18.06	3.03	2.56	9.83	5.08
NGC 1427	1416 ± 10	31.52	-19.71	3.51	2.26	10.66	7.56
IC 2006	1371 ± 12	31.52	-19.27	3.45	2.22	10.39	5.75
NGC 1453	3886 ± 6	33.59	-21.33	3.85	2.21	11.43	10.34
NGC 1600	4688 ± 8	34.06	-22.23	4.17	1.94	11.83	11.25
NGC 1700	3895 ± 7	33.31	-21.30	3.73	2.47	11.11	4.75
NGC 2300	1938 ± 7	32.15	-20.38	3.65	2.23	11.12	12.25
NGC 2778	2060 ± 7	31.88	-18.67	3.34	2.16	10.38	10.94
NGC 3377	724 ± 7	30.33	-19.26	3.28	2.49	10.02	2.89
NGC 3379	945 ± 7	30.20	-20.02	3.27	2.74	10.55	5.88
NGC 3608	1222 ± 7	31.88	-20.19	3.61	2.24	10.77	6.60
NGC 3818	1708 ± 10	32.88	-20.41	3.58	2.33	10.73	5.30
NGC 4261	2238 ± 7	32.58	-21.22	3.79	2.30	11.38	9.87
NGC 4374	1060 ± 6	31.40	-21.39	3.68	2.51	11.25	7.50
NGC 4472	980 ± 10	31.14	-21.81	3.93	2.24	11.49	7.67
NGC 4478	1365 ± 7	31.37	-19.16	3.11	2.85	9.99	2.64
NGC 4489	970 ± 10	31.34	-18.46	3.46	1.91	9.47	1.39
NGC 4552	364 ± 7	31.01	-20.44	3.36	2.71	10.83	7.77
NGC 4649	1117 ± 6	31.21	-21.51	3.80	2.36	11.45	9.87
NGC 4697	1307 ± 10	30.43	-20.36	3.65	2.24	10.73	4.97
NGC 5638	1649 ± 6	32.18	-20.12	3.65	2.17	10.70	5.23
NGC 5812	1929 ± 7	32.23	-20.40	3.47	2.54	10.74	5.65
NGC 5813	1954 ± 7	32.62	-21.20	3.90	2.07	11.19	6.61
NGC 5831	1655 ± 5	32.25	-19.94	3.57	2.22	10.64	6.05
NGC 5846	1714 ± 5	32.06	-21.15	4.02	1.90	11.38	8.96
NGC 6127	4700 ± 10	33.95	-21.03	3.82	2.16	11.24	8.77
NGC 6702	4728 ± 5	33.59	-20.55	3.87	1.94	11.01	6.97
NGC 6703	2403 ± 7	32.18	-20.21	3.50	2.45	10.69	5.49
NGC 7052	4672 ± 8	33.83	-21.14	3.96	1.88	11.50	15.96
NGC 7454	2051 ± 7	31.97	-19.34	3.49	2.16	10.21	3.63
NGC 7562	3608 ± 5	33.87	-21.50	3.86	2.29	11.31	6.42
NGC 7619	3762 ± 5	33.70	-21.77	3.93	2.19	11.55	9.91
NGC 7626	3405 ± 4	33.09	-21.03	3.88	2.05	11.36	10.95
NGC 7785	3808 ± 5	33.32	-20.91	3.78	2.22	11.21	8.47

NOTE.—Col. (1): Galaxy name. Col. (2): Heliocentric radial velocity from González (1993) or Kuntschner (1998). Col. (3): CMB-frame distance modulus from SBF measurements (Tonry et al., in prep.) or flow-corrected models (Tonry et al., priv. comm.). Col. (4): Absolute B magnitude, computed from B_T^0 in Table 2a, col. (4) and the distance in col. (3) here. Col. (5): Logarithm of the effective radius in parsecs. Col. (6): Logarithm of mean B surface brightness inside r_e in solar luminosities per parsec² ($I_e = 10^{-0.4(\mu_e - 27.0)}$; see Bender, Burstein & Faber 1992). Col. (7): Logarithm of the galaxy mass within the effective radius, in solar masses. Computed as $M = 465\sigma_0^2 r_e M_\odot$ (Burstein et al. 1997). Col. (8): Mass-to-light ratio within the effective radius in the B band. Computed as $M/L = 146\sigma_0^2/(I_e r_e) M_\odot/L_\odot$ (González 1993; Burstein et al. 1997).

TABLE 3
UBV PHOTOMETRY FROM LITERATURE

Name	B_T^O	$(U-V)_T^O$	$(U-V)_e^O$	$(U-V)_g^O$	$(B-V)_T^O$	$(B-V)_e^O$	$(B-V)_g^O$
NGC 221	8.72	1.28	1.31	1.46	0.88	0.89	0.94
NGC 224	5.58	0.99	0.68
NGC 315	11.87	1.49	1.53	1.68	0.93	0.96	1.01
NGC 507	12.13	1.41	1.47	1.62	0.91	0.93	0.98
NGC 547	12.92	...	1.43	1.58	...	0.95	1.01
NGC 584	11.21	1.38	1.44	1.59	0.91	0.92	0.97
NGC 636	12.22	1.36	1.41	1.56	0.90	0.91	0.96
NGC 720	11.13	1.44	1.51	1.66	0.96	0.97	1.02
NGC 821	11.72	...	1.52	1.67	0.93	0.94	0.99
NGC 1336	13.08	1.07	1.13	1.28	0.82	0.83	0.88
NGC 1339	12.50	1.41	1.46	1.61	0.92	0.93	0.98
NGC 1351	12.48	1.23	1.33	1.48	0.87	0.91	0.96
NGC 1373	14.08	1.18	0.85
NGC 1374	12.01	1.38	1.44	1.59	0.91	0.93	0.98
NGC 1379	11.87	1.26	1.32	1.47	0.88	0.90	0.95
NGC 1399	10.44	1.46	1.54	1.69	0.95	0.97	1.02
NGC 1404	10.98	1.52	1.55	1.70	0.95	0.97	1.02
NGC 1419	13.46	1.21	1.26	1.41	0.88	0.89	0.94
NGC 1427	11.81	1.33	1.35	1.50	0.90	0.91	0.96
IC 2006	12.25	1.31	1.39	1.54	0.91	0.94	0.99
NGC 1453	12.26	1.53	1.58	1.73	0.96	0.98	1.03
NGC 1600	11.83	1.50	1.57	1.72	0.95	0.97	1.02
NGC 1700	12.01	1.40	1.46	1.61	0.91	0.92	0.97
NGC 2300	11.77	1.66	1.68	1.83	1.01	1.02	1.07
NGC 2778	13.21	1.42	1.47	1.62	0.91	0.94	0.99
NGC 3377	11.07	1.14	1.26	1.41	0.84	0.87	0.92
NGC 3379	10.18	1.46	1.52	1.67	0.94	0.96	1.01
NGC 3608	11.69	1.33	1.44	1.59	0.93	0.95	1.00
NGC 3818	12.47	...	1.46	1.61	0.92	0.93	0.98
NGC 4261	11.36	1.50	1.57	1.72	0.97	0.98	1.03
NGC 4374	10.01	1.44	1.49	1.64	0.94	0.95	1.00
NGC 4472	9.33	1.51	1.57	1.72	0.95	0.97	1.02
NGC 4478	12.21	1.33	1.35	1.50	0.88	0.89	0.94
NGC 4489	12.88	1.10	1.23	1.38	0.83	0.86	0.91
NGC 4552	10.57	1.47	1.55	1.70	0.94	0.96	1.01
NGC 4649	9.70	...	1.61	1.76	0.95	0.98	1.03
NGC 4697	10.07	1.28	1.37	1.52	0.89	0.92	0.97
NGC 5638	12.06	1.34	1.39	1.54	0.91	0.92	0.97
NGC 5812	11.83	...	1.51	1.66	0.94	0.94	0.99
NGC 5813	11.42	1.46	1.51	1.66	0.94	0.95	1.00
NGC 5831	12.31	1.47	1.49	1.64	0.92	0.93	0.98
NGC 5846	10.91	1.41	1.52	1.67	0.96	0.98	1.03
NGC 6127	12.92	0.96	0.97	1.02
NGC 6702	13.04	1.37	1.49	1.64	0.89	0.94	0.99
NGC 6703	11.97	1.40	1.46	1.61	0.91	0.93	0.98
NGC 7052	12.69
NGC 7454	12.63	1.19	1.29	1.44	0.89	0.90	0.95
NGC 7562	12.37	1.58	1.61	1.76	0.98	0.99	1.04
NGC 7619	11.93	1.51	1.59	1.74	0.96	0.98	1.03
NGC 7626	12.06	1.52	1.56	1.71	0.98	0.99	1.04
NGC 7785	12.41	1.48	1.59	1.74	0.96	0.97	1.02

NOTE.—All colors and magnitudes have been corrected for Galactic absorption and redshift. Col. (1): Galaxy name. Col. (2): Total B magnitude from the RC3 for all galaxies except NGC 547 (Poullain & Nieto 1994) and the NGC 224 bulge (Faber et al. 1997). Col. (3): Total $(U-V)$ color from RC3. Col. (4): Effective $(U-V)$ color at r_e from RC3 for all galaxies except NGC 547, NGC 3818, NGC 5812 (Poullain & Nieto 1994), and NGC 821 (Poullain 1988). Col. (5): Central $(U-V)$ color within $r_e/8$ extrapolated inward from $(U-V)_e^O$ using mean logarithmic radial gradients from Peletier et al. (1990) and Goudfrooij et al. (1994) (Section 2.4). Col. (6): Total $(B-V)$ color from RC3. Col. (7): Effective $(B-V)$ color at r_e from RC3 for all galaxies except NGC 547 (Poullain & Nieto 1994). Col. (8): Central $(B-V)$ color within $r_e/8$ extrapolated inward from $(B-V)_e^O$ using the mean logarithmic radial gradient from Goudfrooij et al. (1994) (Section 2.4).

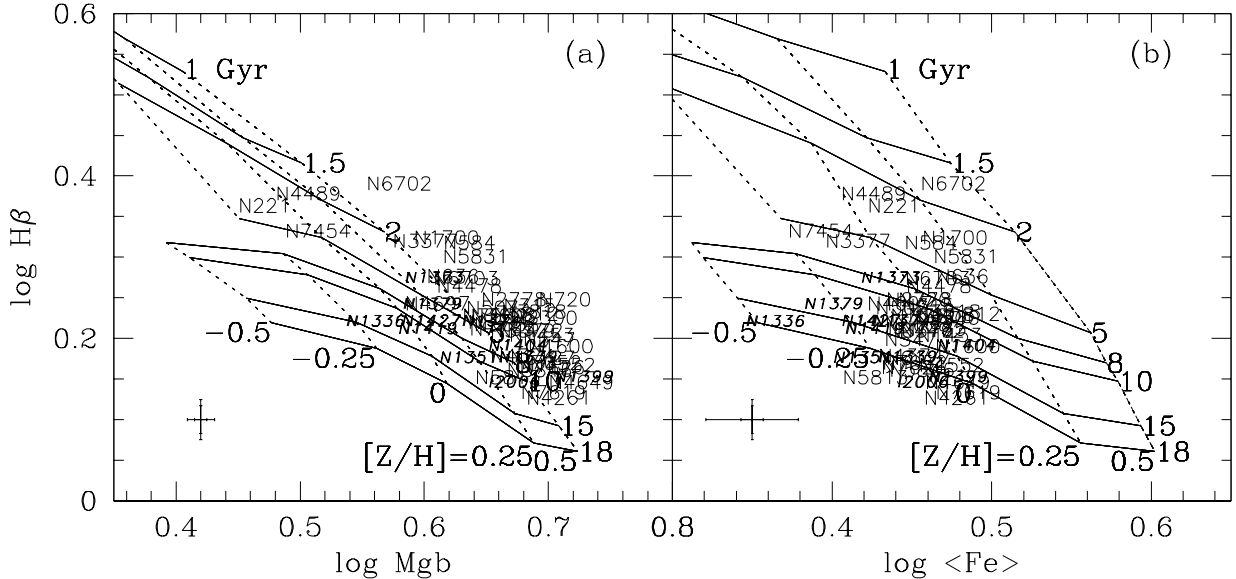


FIG. 1.— Line strengths of G93 (roman type; smaller error bars) and Fornax ellipticals (slanted bold type; larger error bars) through the central $r_e/8$ aperture. Solar-ratio model grids from Worthey (1994) have been superimposed: solid lines are contours of constant age (from top, 1, 1.5, 2, 5, 8, 10, 15, 18 Gyr), and dotted lines are contours of constant $[Z/H]$ (from left, $[Z/H] = -0.5, -0.25, 0.0, +0.25, +0.5$ dex, except at ages younger than 8 Gyr, where from left $[Z/H] = -0.225, 0.0, +0.25, +0.5$ dex). (a) Mgb and $H\beta$ line strengths. (b) $\langle Fe \rangle$ and $H\beta$ line strengths. Differences in the ages and metallicities inferred from the two diagrams result from the non-solar abundance ratios of giant elliptical galaxies. Our procedure corrects for this, and in so doing derives the non-solar abundance ratio, $[E/Fe]$.

3. THE MANIFOLD OF STELLAR POPULATIONS OF LOCAL ELLIPTICAL GALAXIES

3.1. Principal component analysis

This section explores the general landscape of correlations among central SSP-equivalent population parameters (age, metallicity, enhancement ratio, and iron abundance) and the corresponding structural parameters of the parent galaxies. We show below that, among the structural variables, only velocity dispersion correlates significantly with the stellar populations. Furthermore, $[Fe/H]$ can be derived from $[Z/H]$ and $[E/Fe]$. Hence, this section explores the space of the four remaining significant variables t , $[Z/H]$, $[E/Fe]$, and σ .

As an exploratory means of finding the number of independent parameters in this four-dimensional space, we have performed a principal component analysis (PCA; see, e.g., Faber 1973) on the four variables $\log t$, $[Z/H]$, $[E/Fe]$, and $\log \sigma$. The results are presented in Table 4, where it is shown that the first two principal components contain 91% of the variance. Thus, to high accuracy, these local ellipticals are confined to a *two-dimensional surface*, which we propose to call the “metallicity hyperplane.” Figure 2 shows edge-on and face-on views of this plane; $\log \sigma$ and $[E/Fe]$ are the primary contributors to the first principal component, while t and $[Z/H]$ drive the second principal component.

The face-on view of the plane is instructive. First, $[E/Fe]$ and σ are nearly coincident. This is equivalent to saying that one can substitute for the other, i.e., that they are highly correlated. Second, t , σ , and $[Z/H]$ are all moderately orthogonal to one another, and therefore any one of them can be reasonably well represented by a linear combination of the other two. We choose to regard σ and t as independent (see below) and to express $[Z/H]$ and $[E/Fe]$ in terms of them. Hence, to the extent that the thickness of the plane can be ignored, we pre-

dict the following linear relations: $[Z/H] = f(\log t, \log \sigma)$ and $[E/Fe] = g(\log \sigma)$. These are confirmed below. In summary, to present accuracy and based on $H\beta$, Mgb , and $\langle Fe \rangle$ alone, the stellar populations of these local ellipticals are basically a *two-parameter family* determined mainly by velocity dispersion, σ , and SSP-equivalent age, t .

The choice of σ and t as independent variables is not mandated by principal components, which only reveals correlations but cannot show which parameters are fundamental. The dispersion σ was chosen as one independent parameter because it is external to the stellar populations and might plausibly play a causal role in their formation. The selection of t as the second parameter is less obvious. However, since $[Z/H]$ and $[E/Fe]$ evolve as stars form, it seems natural to specify them as functions of time rather than the other way round. In the end, the choice of σ and t as the physically meaningful, “independent” variables is somewhat arbitrary.

3.2. The Z-plane

Fitting directly now for the planar function $[Z/H] = f(\log t, \log \sigma)$, we find:

$$[Z/H] = 0.76 \log \sigma - 0.73 \log t - 0.87, \quad (8)$$

$$\pm 0.13 \quad \pm 0.06 \quad \pm 0.30$$

with an RMS residual of 0.09 dex in $[Z/H]$. (The coefficients have been determined using the “orthogonal fit” procedure of Jørgensen, Franx & Kjaergaard 1996, as coded by D. Kelson; the errors have been estimated using a bootstrap of 1000 replacement samples.) A similar plane was found previously by Trager (1997) for the G93 sample using an older version of SSP parameters that solved for $[E/Fe]$ rather crudely; essentially the same results were obtained. An edge-on view of this plane is

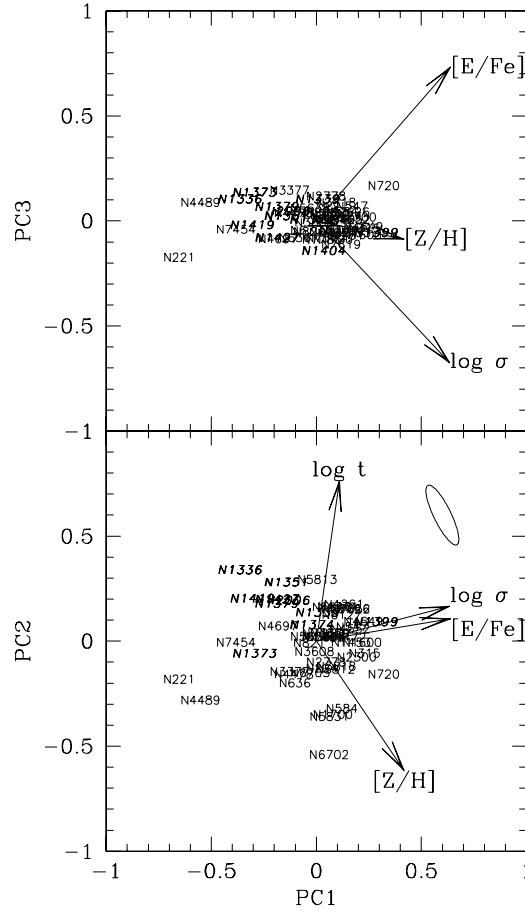


FIG. 2.— The metallicity “hyperplane” of stellar populations of local elliptical galaxies. Fornax ellipticals are shown in bold, slanted type; G93 ellipticals are shown in roman type. Ellipticals populate a plane in metallicity hyperspace, t – $[Z/H]$ – $[E/Fe]$ – σ . The lower panel shows the plane face on. Projections of the four basic variables are shown as arrows in the direction of increase (for $\log t$, this arrow points in the direction of older galaxies). Velocity dispersion and enhancement ratio dominate the first principal component, while age and metallicity dominate the second. The third and fourth principal components contribute less than 10% to the overall variance in t – $[Z/H]$ – $[E/Fe]$ – σ space; the “long axis” (PC1–PC3) of the hyperplane is shown in the upper panel. A 1σ error ellipse typical of the G93 sample is shown in the upper right corner of the lower panel.

TABLE 4
PRINCIPAL COMPONENT ANALYSIS

Variable	PC1	PC2	PC3	PC4
σ'	0.64	0.16	-0.68	0.34
t'	0.11	0.76	-0.03	-0.64
z'	0.42	-0.62	-0.09	-0.66
e'	0.64	0.11	0.73	0.21
Eigenvalue	2.02	1.63	0.27	0.07
Percentage of variance	50	41	7	2
Cumulative percentage	50	91	98	100

NOTE.—Primed variables are “reduced” versions of the corresponding variables with zero mean and unit variance:

$$\begin{aligned}\sigma' &= (\log \sigma - 2.27)/1.29, \\ t' &= (\log t - 0.88)/1.82, \\ z' &= ([Z/H] - 0.21)/1.29, \\ e' &= ([E/Fe] - 0.18)/0.47.\end{aligned}$$

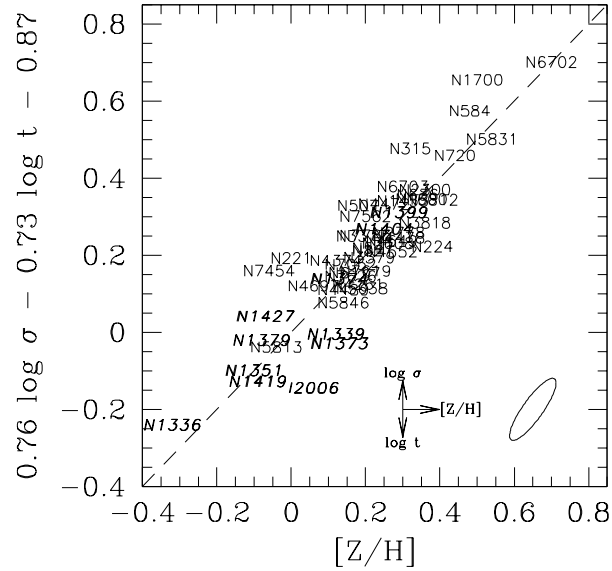


FIG. 3.— An edge-on view of the Z-plane in hyperspace (points as in Figure 1). The dashed line is the line defining the plane (Eq. 8). Vectors of $\Delta \log \sigma = +0.1$, $\Delta \log t = +0.1$ (i.e., 26% older), and $\Delta [Z/H] = +0.1$ dex are shown at bottom, along with a typical error ellipse for the G93 sample.

shown in Figure 3, and the face-on view is shown in Figure 4. We call this plane the “Z-plane.”

We stated above that σ is the only structural variable that correlates with stellar population parameters. More precisely, we mean that adding more structural parameters to fits of the form $[Z/H] = f(\log t, \log \sigma, \log r_e, \log I_e)$ (where r_e is effective radius and I_e is effective surface brightness) does not significantly reduce the scatter in $[Z/H]$. While $[Z/H]$ should correlate with mass or luminosity through its correlation with σ , substituting mass or luminosity for $(\log \sigma, \log r_e)$ and $(\log \sigma, \log r_e, \log I_e)$ respectively in the fits actually increases the scatter in $[Z/H]$. This implies that the basic correlation is through σ .

The existence of the Z-plane says that there exists an *age–metallicity relation* for each value of σ . Contours of constant σ are shown in Figure 4 and have slope $\Delta \log t = -1.4 \Delta [Z/H]$. This is very close to the “3/2 relation” of Worthey (1992, 1994), which expresses trajectories in $\log t$ – $[Z/H]$ space along which colors and line strengths remain roughly constant. Thus, following Trager (1997), we predict that line strengths should be constant along trajectories of constant σ in the Z-plane, an important conclusion to which we will return in Section 5.2.

3.3. The $[E/Fe]$ – σ relation

PCA analysis indicates that the enhancement ratio, $[E/Fe]$, is closely coupled to the velocity dispersion, with $[E/Fe]$ increasing as σ . Figure 5 confirms this close relationship. The dashed line is a linear least-squares fit of the form

$$[E/Fe] = 0.33 \log \sigma - 0.58, \quad (9)$$

$$\pm 0.01 \quad \pm 0.01$$

with an RMS residual of 0.05 dex. Adding other structural parameters ($\log r_e$ and $\log I_e$) to the fit again does not reduce the scatter significantly, nor does replacing $(\log \sigma, \log r_e)$ with mass. Replacing $(\log \sigma, \log r_e, \log I_e)$ with luminosity—i.e., fits of the form $[E/Fe] = f(\log L)$ —actually increases the scatter slightly. Thus, although $[E/Fe]$ obviously correlates loosely with other structural variables such as mass and luminosity, the basic correlation is through σ . It will be noted that outlying galaxies from the $[E/Fe]$ – σ relation also lie off the plane in the upper panel of Figure 2. Hence, from Table 4, scatter in the $[E/Fe]$ – σ relation must reflect the role of PC3 in thickening the hyperplane. The scatter is larger than the error bar in Figure 5, indicating that $[E/Fe]$ does not correlate perfectly with σ ; the same point was made also by Kuntschner (1998). Clearly, the hyperplane has some finite thickness, and the statement that the galaxies are a two-dimensional manifold is only approximate.

3.4. The Fe-plane

For completeness we also plot $[Fe/H]$ as a function of t and σ in Figure 6. Since $[Fe/H]$ is closely equal to $[Z/H]$ – $[E/Fe]$ and $[E/Fe]$ is a function of σ only, we predict a plane analogous to the Z-plane, but with different slope. Indeed, such a plane is found, with equation:

$$[Fe/H] = 0.48 \log \sigma - 0.74 \log t - 0.40, \quad (10)$$

$$\pm 0.12 \quad \pm 0.09 \quad \pm 0.25$$

and with an RMS residual of 0.08 dex. $[Fe/H]$ is even tighter vs. age than $[Z/H]$ (compare Figure 6 with Figure 4). This tightness is due to the dependence of $[E/Fe]$ on σ , which causes Fe to rise more slowly than $[Z/H]$ vs. σ , and thus compresses the spread in Fe at fixed time. Mathematically, the Fe-plane is “flatter” in velocity dispersion than the Z-plane.

3.5. The effect of observational errors

It is important to examine the role that observational errors play in creating the above correlations, particularly the Z- and Fe-planes. From Figure 1, it is evident that an error in any one of the observed quantities $Mg b$, $\langle Fe \rangle$, or $H\beta$ will cause correlated errors in the output quantities $[Z/H]$, $[E/Fe]$, and t . However, $H\beta$ is the most critical index, and errors in it are the most dangerous. Moving $H\beta$ up in Figure 1 causes age to decline and $[Z/H]$ to increase ($[E/Fe]$ is less affected). This correlated error is responsible for the long axis of the tilted error ellipses in the two plane diagrams, Figures 4 and 6. Note that these ellipses point almost directly parallel to the claimed trends in age at fixed σ . Note further that the error ellipse in Figure 3 is parallel to the edge-on view of the Z-plane, indicating that errors do not significantly broaden the plane (the same is true of the Fe-plane though no edge-on view is shown). Hence, it is possible for errors, if they are big enough, to create the *impression* of planes by broadening a distribution that is intrinsically merely a one-dimensional line. For example, all ellipticals might be the same age, obey the $[E/Fe]$ – σ relation (a line), and be broadened by large $H\beta$ errors to fill apparent “planes” just like those observed.

The only defense against such an error is to know from independent measurements that the observational errors are small. That is why we use only the G93 and Kuntschner (1998) samples, whose errors are small and well understood. The rms error of $H\beta$ in G93 is 0.060 Å, and in Kuntschner (1998) is 0.089 Å, with errors in the other indices being comparable. As shown by the error ellipses in the figures, these errors are small enough that the observed planes cannot be artifacts. Much larger errors, however, would be disastrous. For example, Figure 4 also shows the error ellipse for a typical galaxy in the IDS sample of TWFBG98 ($\sigma_{H\beta} = 0.191$ Å for the 150 highest-quality galaxies). Monte Carlo simulations of this sample (Trager 1997) have shown that the observed $[Z/H]$ - and Fe-planes were largely artifacts caused by observational errors; this is consistent with the large size of the IDS error ellipse in Figure 4. A reasonable guide is that $H\beta$ must be accurate to ~ 0.1 Å to measure reliable ages and metallicities.

3.6. Comparison with previous studies

We compare next to other studies using Balmer-line data to determine stellar population parameters. The study by Kuntschner (1998) on Fornax ellipticals is quite consistent with ours, which is not surprising since we use the same data and similar models. Kuntschner’s conclusions were limited by the fact that his corrections for non-solar abundance ratios were only approximate. Nevertheless, his findings that the Fornax ellipticals are mainly old and that they show a strong $[E/Fe]$ – σ relation are confirmed here.

The study by Jørgensen (1999) of 71 early-type galaxies in Coma is similar in both approach and conclusions to the present work. Jørgensen (1999) analyzed newly obtained long-slit and multi-fiber spectra and derived stellar population parameters using line-strength models by Vazdekis et al. (1996). Overall her findings are similar to ours, including a $\log \sigma$ – $[Mg/Fe]$ relation like that in Figure 5, an age– $[Mg/H]$ relation rather like that in Figure 4, and a tight age– $[Fe/H]$ relation nearly identical to that in Figure 6.

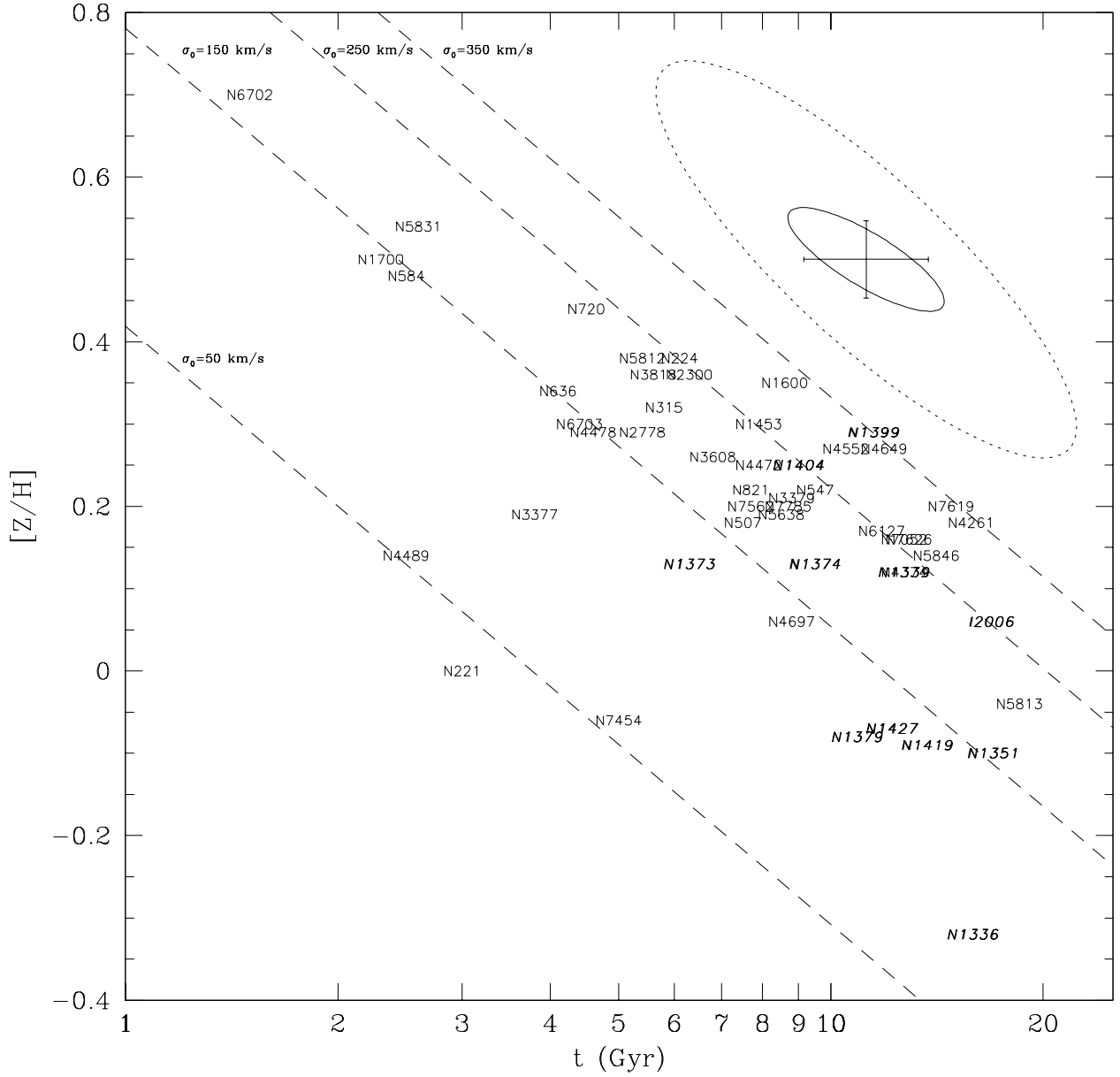


FIG. 4.— A face-on view of the Z-plane in hyperspace (points as in Figure 1). At fixed velocity dispersion (dashed lines), younger galaxies have higher metallicities than older galaxies. The solid error ellipse in the upper right-hand corner is typical of the G93 sample; the dotted ellipse is typical of the highest quality data in the Lick/IDS galaxy sample (Trager et al. 1998). The slope of the error ellipses is nearly identical to the slope of lines of constant velocity dispersion, indicating that poor data can masquerade as real trends.

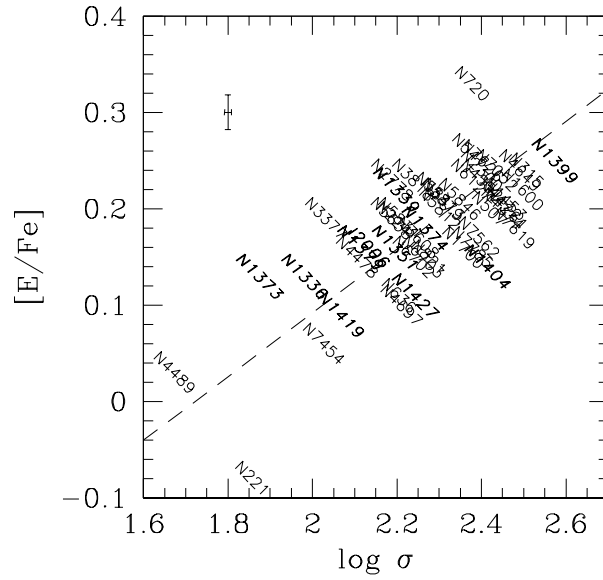
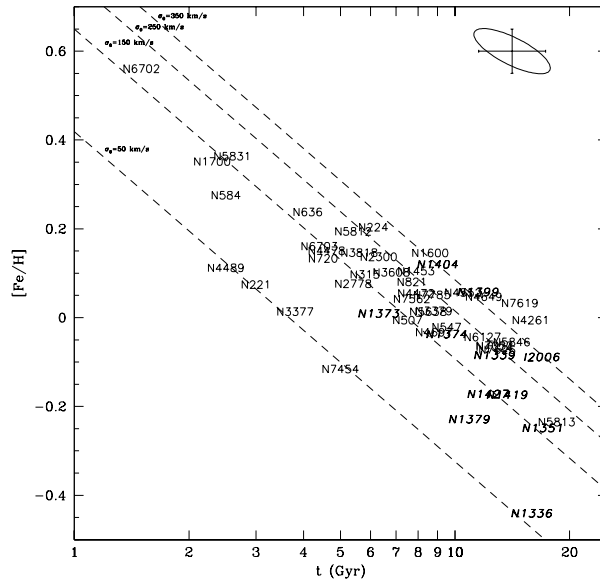


FIG. 5.— The $[E/Fe]$ - σ relation for local ellipticals (points as in Figure 1). High values of $[E/Fe]$ actually reflect low values of $[Fe/Z]$ rather than high $[E/Z]$ (see text). The dashed line is a least-squares fit to the relation of the form $[E/Fe] = 0.33 \log \sigma - 0.58$.



However, the typical error of $H\beta$ in the Jørgensen data is 0.22 Å, with a long tail to larger errors. Overall, her data are comparable in accuracy to the IDS data of TWFBG98, which were found to be inadequate for age determination by Trager (1997). Given our present understanding of the pernicious effects of errors (Section 3.5), we suspect that some of the trends found by Jørgensen are real but that others may be largely artifacts caused by errors. Specifically, the $\log \sigma$ – $[\text{Mg}/\text{Fe}]$ relation found by Jørgensen is almost certainly correct, whereas any of the relations involving age (including both the Z -plane and the Fe -plane) are likely to be heavily contaminated. A high-accuracy line-strength survey of Coma ellipticals is badly needed.

The study of Tantalò, Chiosi & Bressan (1998a) analyzed G93 data and is thus relatively unaffected by observational errors. A detailed comparison to this work was made in Paper I. The methodology of these authors is very similar to ours except that only $\text{Mg } b$ is corrected for non-solar ratios whereas $\langle \text{Fe} \rangle$ is unchanged. Their method essentially measures $[\text{Z}/\text{H}]$ based on $\langle \text{Fe} \rangle$ alone, and metallicities are consequently underestimated and enhancements overestimated, by amounts that increase with $[\text{E}/\text{Fe}]$.

Systematic errors increasing with $[\text{E}/\text{Fe}]$ introduce slope errors into most correlations. For example, TCB98 find a strong $[\text{E}/\text{Fe}]$ –age relation, which seems to be our $[\text{E}/\text{Fe}]$ – σ relation lensed through correlated errors. The importance of this discussion is to show that the factors used to correct line strengths for non-solar abundance ratios—in particular the *relative amplitudes* of the corrections to $\text{Mg } b$ and $\langle \text{Fe} \rangle$ —have far-reaching consequences for parameter correlation studies. Our corrections are based self-consistently on the TB95 response functions, but independent checks of those functions would be welcome.

4. OTHER PROJECTIONS OF THE METALLICITY HYPERPLANE

The notion that the stellar-population manifold of elliptical galaxies is inherently two-dimensional is key to understanding many two-parameter relationships involving these galaxies. Most such relationships are either projections of this higher-dimensional space or are close relatives of such projections. The slope and scatter of points in such projections are not fundamental, but rather depend on the distribution of points within the hyperplane. The question of sample selection thus enters acutely, as that may govern the distribution of points in the plane.

4.1. The velocity dispersion–age projection

Figure 7 shows several examples of how two-dimensional projections are affected by the distribution of points in the hyperplane. Points are coded by the environment of each galaxy in preparation for the discussion of environmental effects in the next section.

Figure 7a (upper left panel) shows the independent variables σ vs. t . Since the (σ, t) distribution governs the appearance of all other projections, it is interesting to compare the distributions within it of galaxy subsamples classed by environment; isolated, group, and cluster ellipticals are shown by open circles, small dots, and large dots respectively. These distributions look rather different; cluster E’s (large filled circles) are grouped near the top of the plot, except for three young outliers shown by the labeled points: NGC 1373 is a bona fide member of Fornax based on position and velocity yet is conspicuously young, the only young Fornax elliptical; NGC 4489 is 4 degrees from the center of Virgo but is a member by radial velocity. It,

too, is rather young, as is NGC 4478, which is right near the center of Virgo and is clearly a cluster member. Within the errors, however, the bulk of cluster galaxies is consistent with being old and coeval.

Group and isolated objects (which we collectively term “field” ellipticals; small dots and open circles) are distributed differently from cluster ellipticals in the hyperplane. They cover a larger age range, and there is a weak trend in t vs. σ in the sense that low- σ galaxies tend to be younger; the clump of old, low- σ galaxies that is prominent among the cluster galaxies is also missing.

We conclude that the (σ, t) distributions of local field and cluster ellipticals differ in the present sample, and that their two-parameter projections may also differ on that account. That prediction is explored in the following panels.

4.2. The σ – Z projection

Figure 7b (lower left panel) plots $[\text{Z}/\text{H}]$ vs. σ . A velocity dispersion–metallicity relation appears to exist for old cluster galaxies, but the three young cluster galaxies NGC 1373, NGC 4489, and NGC 4478 lie at higher $[\text{Z}/\text{H}]$ at given σ . No comparable relation appears to exist for field ellipticals. This difference is a natural consequence of the differences in the (σ, t) distributions above. This projection is a close relative of the classic mass–metallicity relation and is discussed further in Section 5.1.

4.3. The t – $[\text{E}/\text{Fe}]$ projection

Figure 7c (upper right panel) shows the distribution of $[\text{E}/\text{Fe}]$ as a function of age. There is no apparent trend in $[\text{E}/\text{Fe}]$ with t in any sample. This is as expected, since we found earlier that $[\text{E}/\text{Fe}]$ depends only on σ and not on t .

4.4. The Z – $[\text{E}/\text{Fe}]$ projection

Figure 7d (lower right panel) shows the distribution of $[\text{E}/\text{Fe}]$ as a function of metallicity $[\text{Z}/\text{H}]$. There is a weak tendency for $[\text{E}/\text{Fe}]$ to increase with $[\text{Z}/\text{H}]$, especially among old cluster ellipticals, suggesting higher SNe II/SNe Ia enhancement ratios in higher-metallicity galaxies. This trend among old cluster E’s is again expected from their narrow age distribution in Figure 4—in a narrow age range, $[\text{Z}/\text{H}]$ increases with increasing σ , and therefore $[\text{E}/\text{Fe}]$ should increase with $[\text{Z}/\text{H}]$ at fixed t .

4.5. Summary of results

Our results so far can be summarized as follows. A principal component analysis demonstrates that central stellar populations in the present sample of local elliptical galaxies can be largely specified using just two independent variables; we take these to be SSP-equivalent age, t , and velocity dispersion, σ . Velocity dispersion is the only structural parameter that appears to play a role in modulating the stellar populations of these galaxies.

This two-dimensional “metallicity hyperplane” is in turn comprised of two sub-relations: metallicity is a linear function of both t and σ , which we call the “ Z -plane,” and enhancement ratio, $[\text{E}/\text{Fe}]$, is a linear function of σ , increasing towards high- σ galaxies. Together these two subrelations comprise the hyperplane.

Several caveats are necessary. First, the thickness of the hyperplane appears to be at least partly real and is associated

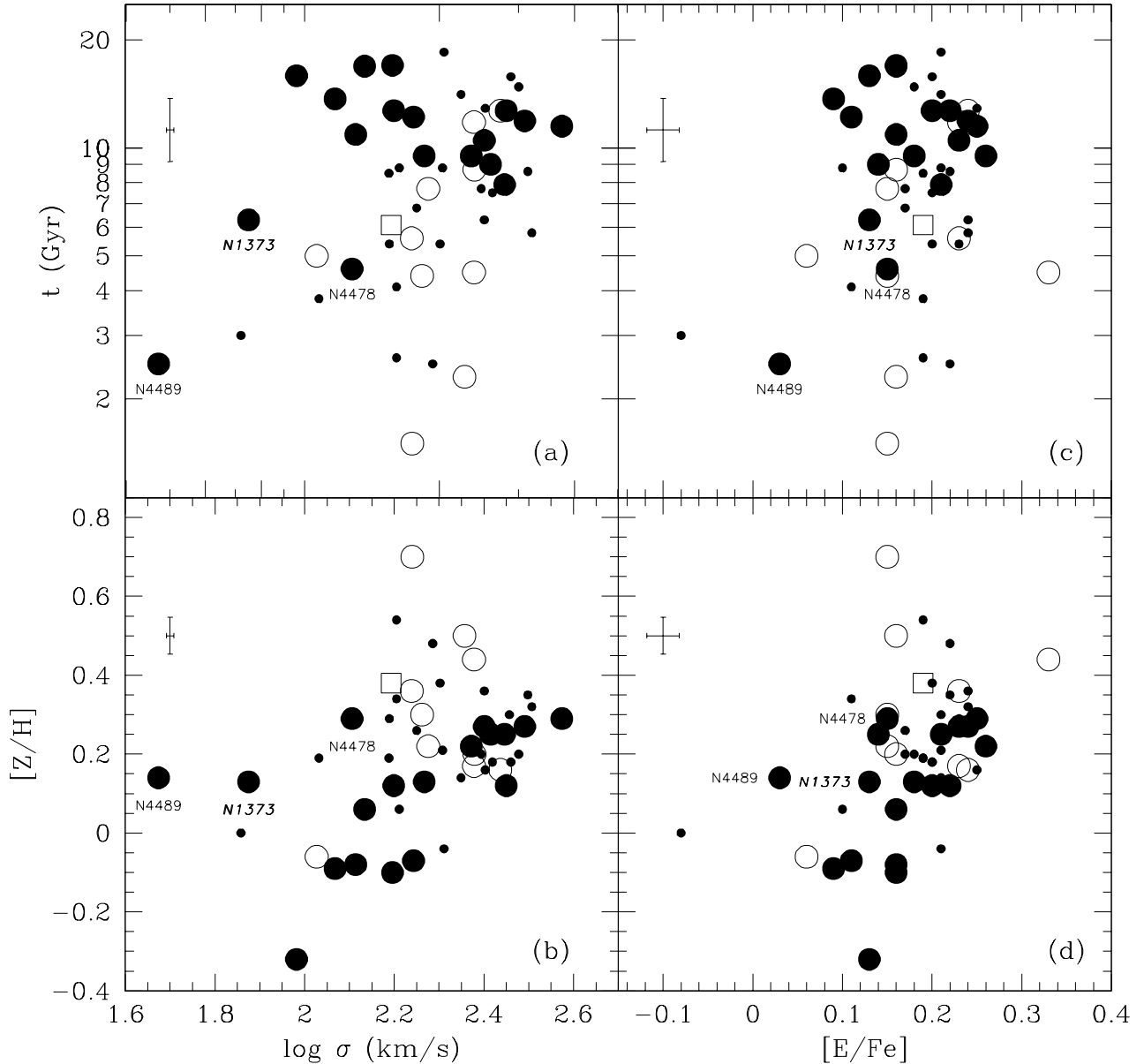


FIG. 7.— Two-dimensional projections of the metallicity hyperplane, coded by galaxy environment. The figure illustrates how the distribution of points in the Z -plane affects projected correlations. Group assignments and group richnesses are taken from Faber et al. (1989) for most galaxies. Large filled circles are cluster galaxies (Virgo and Fornax); small filled circles are group galaxies; open circles are isolated galaxies; and the large open square represents the center of NGC 224 (M 31). (a) The independent variables σ – t , showing the different distributions of various subsamples in the hyperplane. Most cluster galaxies (large filled circles) are old (with the notable exceptions of the small galaxies NGC 4489, NGC 1373, and NGC 4478), whereas field galaxies (groups + isolated objects) span a large range in ages. (b) The σ – $[Z/H]$ projection. With the exception of the three outliers, cluster galaxies trace a fairly well defined metallicity– σ relation; field galaxies do not. (c) The $[E/Fe]$ – t projection. No clear trends are seen in any subsamples. (d) The $[E/Fe]$ – $[Z/H]$ projection. A slight hint of an increase of $[E/Fe]$ with $[Z/H]$ is apparent, but the scatter is large.

mainly with scatter in the $[E/Fe]-\sigma$ relation. Thus, the populations are not perfectly two-dimensional, and at least one more factor must play a role. Second, the present SSP parameters are based on only three spectral indices (Mgb , $\langle Fe \rangle$, and $H\beta$), and adding more indices (or colors) might reveal more principal components; we will be investigating this in future papers. Third, coverage of the hyperplane needs to be improved by adding more young populations, which are relatively scarce here. Fourth, the present data refer to only 51 galaxies; a larger sample is needed to confirm that the present trends in fact apply to local elliptical galaxies generally. Fifth, we must remember that the hyperplane refers to *SSP-equivalent* population parameters, which are disproportionately influenced by young stars (see Appendix). However, despite the fact that SSP-parameters are not true mass-weighted averages, they still place very tight constraints on the history of star formation in ellipticals, as shown below in Sections 6 and 7.

Finally, the present analysis delineates the position and orientation of the hyperplane in hyperspace but says little about the distribution of galaxies within it. That is because our sample does not constitute an unbiased *volume-limited* sample of local ellipticals. This places severe limits on our conclusions. For example, we cannot conclude that the wide range of SSP ages seen in our field galaxies is typical of local field ellipticals generally. However, there is a strong suggestion in our data that the (σ, t) distributions of field and cluster galaxies may differ, with cluster ellipticals in the present sample being generally older. This difference is expected to generate environmental differences in the two-dimensional projected scaling laws of these galaxies, as explored in the next section.

5. TWO CLASSICAL SCALING LAWS

This section investigates two classical scaling laws for elliptical galaxies: the mass-metallicity relation and the $Mg-\sigma$ relation. Both can be understood as two-dimensional projections of the metallicity hyperplane.

5.1. The mass-metallicity relation: environmental effects

Environmental differences among elliptical galaxies have generated intense interest (e.g., de Carvalho & Djorgovski 1992; Burstein, Faber & Dressler 1990; Gúzman et al. 1992; Bernardi et al. 1998). We consider here their impact on a question of major importance, the mass-metallicity relation of elliptical galaxies, widely regarded as a key clue to their nucleosynthetic histories (e.g., Aaronson & Mould 1985). The relation comes in several guises: $[Z/H]$ vs. mass, $[Z/H]$ vs. luminosity, and $[Z/H]$ vs. σ —this last also counts as a mass-metallicity relation since mass and σ are so closely correlated.

These three projections are compared in Figure 8. The $[Z/H]-\sigma$ projection (panel a) is repeated here from Figure 7. We have already observed that any relation in this panel is weak; old cluster galaxies (large filled circles) show a trend in the classic sense that high- σ galaxies are more metal rich, but this trend is not shared by field galaxies (open circles and small dots). Panels b and c show $[Z/H]$ vs. mass and $[Z/H]$ vs. absolute magnitude (the latter quantities are taken from Table 2b). These relations show even more scatter than $[Z/H]$ vs. σ , and the real mass-metallicity relation (panel b) is worst of all.

It is not our purpose to argue here that there is *no* mass-metallicity relation. Rather, like many two-dimensional correlations claimed for elliptical galaxies, the mass-metallicity relation is actually a projection of a higher-dimensional space. As such, it may be both environmentally and sample dependent,

and its accurate determination will require a larger and more carefully controlled sample than we have here.

5.2. The $Mg-\sigma$ relations

The $Mg-\sigma$ relations present a major challenge to the hyperplane model. The tightness of these relations has often been taken as evidence that all ellipticals have nearly coeval stellar populations to of order 15% in age (Bender, Burstein & Faber 1993; Bernardi et al. 1998), in strong contradiction to the spread of about a factor of 10 in SSP ages found in this work. We are planning a separate paper on this important issue but include a short section here in order to address pressing questions that will occur to knowledgeable readers.

Our picture is that the $Mg-\sigma$ relations look narrow because they are edge-on (or nearly edge-on) projections of the metallicity hyperplane. The germ of this idea is contained in Figure 4, which shows the Z-plane face on. Imagine rotating this plane about an axis running perpendicular to the contours of constant σ and viewing the resultant projection edge-on. Suppose further that SSP-equivalent age and metallicity “conspire” to cause Mgb (or Mg_2) to remain sensibly constant along a σ -contour. This would occur if $\Delta \log t / \Delta [Z/H] = -1.7$ or -1.8 (W94), and indeed the Z-plane at fixed σ (Equation 8) has slope very close to this: $\Delta \log t / \Delta [Z/H] = -1.4$. In other words, lines of constant σ closely obey the 3/2 rule, and line-strength along them should be nearly constant. In projection, Mgb and Mg_2 should therefore be tight functions of σ , yielding the $Mg-\sigma$ relations.

To illustrate this graphically, we have performed Monte Carlo simulations to produce Mgb and σ values for roughly 500 “fake” elliptical galaxies realistically distributed in the metallicity hyperplane. Random values of the first two principal components in Table 4 were drawn from the distribution of galaxies in the face-on view of the plane (Figure 2), and the third and fourth components were set identically to zero. These four PCA eigenvectors were then inverted to determine t , $[Z/H]$, $[E/Fe]$, and σ for each realization, and the first three parameters were used to generate line strengths using the formalism described in Paper 1, with typical observational errors added. The resulting simulated $Mgb-\sigma$ relation is shown in Figure 9a. The derived relation (dotted line) has the form

$$\log Mgb = 0.312 \log \sigma - 0.054, \quad (11)$$

$$\pm 0.002 \quad \pm 0.001$$

with an RMS scatter of only 0.007. The $Mgb-\sigma$ relation for the present sample of local elliptical galaxies (dashed line, panel b) has the form

$$\log Mgb = 0.294 \log \sigma - 0.016, \quad (12)$$

$$\pm 0.005 \quad \pm 0.001$$

with an RMS scatter of 0.032 (51 galaxies). The good agreement between the simulated relation and the real one confirms that a large age spread of stellar populations in the hyperplane can indeed be masked by the tendency of $[Z/H]$ to rise at low ages, precisely compensating the effect of age differences.

We briefly mention a few important points, saving details for our future paper:

(1) The idea that the tightness of the $Mg-\sigma$ relations might conceal large age variations was first proposed by Worthey et al. (1996) and was re-proposed by Jørgensen (1999). In both cases, the actual age spreads were probably somewhat overestimated,

as Worthey et al. used the Lick/IDS data while Jørgensen used her Coma sample, both of which contain significant observational errors (Sections 3.5 and 3.6). Nevertheless, the basic correctness of the idea is confirmed here.

(2) While the slopes of the real and simulated $Mgb-\sigma$ relations match well, the scatter in the simulated relation is too small even though observational errors have been included. That is because the third and fourth principal components were neglected, i.e., the hyperplane was taken to be infinitely thin. This was done deliberately to make any residual tilt of the hyperplane more visible. Even with this, the simulated relation is still extremely narrow, showing that any deviation from an edge-on orientation must be small. The larger scatter of the real $Mgb-\sigma$ relation must be due to the presence of PC3 and PC4, which were not included in the simulation. PC3, in particular, reflects real scatter in the $[E/Fe]-\sigma$ relation, as noted in Section 3.3.

(3) Although the $Mg-\sigma$ relations are generally tight, morphologically disturbed ellipticals tend to show lower Mg values than expected, and this has been convincingly interpreted as due to recent star formation by Schweizer et al. (1990) and Schweizer & Seitzer (1992). Comparably young stellar populations are present in some of our galaxies here (e.g., NGC 6702, NGC 5831, NGC 1700), yet none of these shows any significant deviation from $Mgb-\sigma$ in Figure 9. Is this a disagreement?

A full discussion of this point is reserved to our future paper, but we can sketch the answer briefly here. First, the Mg relations used by Schweizer et al. (1990) and Schweizer & Seitzer (1992) actually plotted Mg vs. luminosity, L , not σ . Recent star formation would increase L while depressing Mg, thus amplifying any Mg residual. Second, a handful of low-lying points can be seen in the simulated $Mgb-\sigma$ relation in Figure 9. These turn out to be the youngest galaxies, demonstrating that slight curvature in the transformations back to raw Mgb can cause objects to lie low if they are extremely young. Finally, essentially all previous investigations of $Mg-\sigma$ have used Mg_2 , whereas we chose Mgb because it was more accurately measured by G93. This decision proves to be important, as separate other work now shows that $Mg_2-\sigma$ is not as tight as $Mgb-\sigma$ and does indeed show small but systematic negative residuals for younger stellar populations. This is evident both in the present sample and in the larger Lick/IDS sample of TWFBG98.

Thus, it appears that both views are correct: the basic tightness of the $Mg-\sigma$ relations conceals large age spreads, but Mg_2 in particular deviates systematically in the sense that young stellar populations lie low. Further discussion of these and other aspects of the $Mg-\sigma$ relations will be provided in our future paper.

6. THE ORIGIN OF THE $[E/Fe]-\sigma$ RELATION

We have seen that there are two major correlations involving the stellar populations of the present sample: the Z-plane linking $[Z/H]$, t , and σ ; and the $[E/Fe]-\sigma$ relation linking $[E/Fe]$ and σ . Assuming that these relations are in fact a good description of local ellipticals generally, we attempt to deduce the implications for their star formation histories. To anticipate, we find a number of plausible explanations for $[E/Fe]-\sigma$; the relation is interesting and useful but in retrospect not very surprising. The existence of the Z-plane on the other hand turns out to be very puzzling and may emerge as one of the most telling constraints on the history of star formation in ellipticals. This section focuses on the simpler $[E/Fe]-\sigma$ relation; theories for the Z-plane are explored in the next section.

Six scenarios for $[E/Fe]-\sigma$ are considered; findings are summarized as a truth table in Table 5. Each scenario is compared to three observed trends in a binary, yes-no way—does the scenario account for the observed trend or not? The first trend is the $[E/Fe]-\sigma$ relation itself, which is given highest weight. We also add two additional “trends,” that $[Z/H]$ and $[Fe/H]$ both increase with σ . These trends are true strictly speaking only at fixed t (Equations 8 and 10), and thus apply only to populations with a narrow range of SSP ages, e.g., cluster galaxies. Since all ellipticals are clearly *not* the same SSP age, using these extra trends may be unwarranted. However, adding them narrows the possibilities greatly, and it is perhaps reasonable to require that any successful scenario for the $[E/Fe]-\sigma$ relation must separately explain old cluster galaxies. Most of the ideas below have been discussed in the literature before, but the present information on $[E/Fe]$, $[Z/H]$, and $[Fe/H]$ separately sheds new light.

Strictly speaking, our measurements refer to SSP values of $[E/Fe]$, which are heavily weighted by young stars. However, experiments in Section 7 suggest that mixed-age “frosting” models must have rather constant values of $[E/Fe]$ in all sub-populations in order for composite galaxies to match the Z-plane. In such cases, SSP values of $[E/Fe]$ are a good mass-weighted mean for the whole population.

The scenarios are as follows:

(1) *The number of stellar generations (i.e., total astration) increases with increasing σ .* This scenario has roots in the classic closed box model and envisions that star-formation and cosmic recycling go further at higher σ (assuming that the relative yields from Type Ia and Type II SNe do not change). This scenario can account for higher $[Z/H]$ and $[Fe/H]$ with higher σ but clearly does not predict any change in $[E/Fe]$. It is included for completeness only.

(2) *The duration of star formation is shorter with increasing σ .* This scenario envisions that the total duration of star formation (in years, not in stellar generations) is reduced at high σ (e.g., Worthey, Faber & González 1992). Such shortening would reduce the amount of Fe-peak elements because star formation would be over before SNe Ia exploded and their Fe-peak products became available for incorporation into new stars. In this scenario, total astration through SNe II remains the same, but elements from SNe Ia are reduced. This matches the observed increase in $[E/Fe]$ with σ , but, because total element production is also reduced, it cannot match either the increase in $[Z/H]$ or $[Fe/H]$ with higher σ .

Scenarios 1 and 2 were designed to separate the notion of the *number of generations* of element building (astration) from the *number of years* needed to form those generations (duration). Since the two scenarios have complementary failings in Table 5, one may wonder whether combining them (shorter formation time plus more astration at high σ) might match all the data. This is a quantitative question whose answer depends on detailed model parameters and calculations. Our impression is that such a model could likely match the increase in $[E/Fe]$ and $[Z/H]$ with σ but would probably have flat or falling $[Fe/H]$ vs. σ , contrary to the data. Even more difficult is the fact that, in nature, astration and duration are naturally positively coupled—longer star formation means there is time for more astration—not anti-coupled as in this hybrid model. Such coupling is seen, for example, in the models of Larson (1974), Arimoto & Yoshii (1987), and Thomas, Greggio & Bender (1999). Moreover, in all these cases, as star formation proceeds, recycling of material through SNe Ia causes $[E/Fe]$ to decrease and metallicity

TABLE 5
SCENARIOS FOR THE $[E/Fe]$ - σ RELATION

Scenario	$[E/Fe]$ \uparrow with σ \uparrow ?	$[Z/H]$ \uparrow with σ \uparrow (at fixed t)?	$[Fe/H]$ \uparrow with σ \uparrow (at fixed t)?
1) No. stellar generations increases as σ increases	n	y	y
2) Star formation duration decreases as σ increases	y	n	n
3) Late winds reduce SN Ia yield as σ increases	y	n	n
4) Number of Type Ia SNe decreases as σ increases	y	n	n
5) IMF flattens as σ increases	y	y	y
6) Early winds reduce SN II yield as σ decreases	y	y	y

and $[Fe/H]$ to rise. $[E/Fe]$ is therefore naturally *anti*-correlated with the others, unlike the data. For both reasons, combining scenarios 1 and 2 does not seem promising.

(3) *Late winds are stronger with increasing σ* . This scenario is essentially a carbon-copy of scenario 2 in that both serve to reduce the amount of SN Ia-enriched material retained by the galaxy while leaving SN II products unchanged. Like scenario 2, it matches the increase in $[E/Fe]$ with σ but predicts a fall in both $[Z/H]$ and $[Fe/H]$ at high σ , contrary to observations. Moreover, it is inherently implausible that galactic outflows should be *higher* in high- σ galaxies, which have deeper potential wells.

(4) *The number of Type Ia SNe decreases with increasing σ* . If SNe Ia are explosions of double-degenerate systems as is generally assumed (e.g., Wheeler & Harkness 1990), their progenitors are tight binaries. It may be that, in a high- σ environment, glancing cloud-cloud collisions impart enough angular momentum to form only very wide binaries, and thus suppress the formation of SNe Ia progenitors. Intriguing as this speculation is, the net result of this proposal is again not very different from the previous two scenarios, which reduce elements from SNe Ia while leaving those from SNe II unchanged. It fails for the same reasons.

The next two scenarios *increase* element yields from SNe II while leaving leaving those from SNe Ia unchanged. These are more successful.

(5) *IMF flattens with increasing σ* . In this scenario, more high-mass stars are born and more SNe II are produced in high- σ galaxies, increasing the effective yield and thus the overall mean metal abundance of the stellar population (Tinsley 1980). The quantities $[E/Fe]$, $[Z/H]$, and $[Fe/H]$ all increase with σ (this last because Type II SNe produce at least some Fe; Woosley & Weaver 1995). However, the increase in $[Fe/H]$ should be weaker than in $[Z/H]$, as is observed (compare Equations 8 and 10). Although this scenario matches all the data, no physical mechanism for it is as yet known. Perhaps massive star-formation is enhanced at high cloud-cloud collision velocities, which in turn would scale in rough proportion to stellar velocity dispersion (Faber, Worthey & González 1992).³

(6) *Early winds are stronger with decreasing σ* . In this scenario, all ellipticals produce SN Ia and SN II products at the

same rate, but low- σ galaxies lose their early, SN II-enriched gas more readily than high- σ galaxies (see Vader 1986, 1987 for an early discussion of this process). High- σ galaxies would have a higher effective yield of Type II SNe products, resulting in a positive $[E/Fe]$ - σ relation and, because of their higher retention of Type II SNe products, higher overall metallicities as well. Since Type II SNe make *some* Fe (see above), $[Fe/H]$ should also increase weakly with σ , as is seen. Observationally, abundance trends in this scenario are similar to those of scenario 5, in which the IMF is modulated by σ .

From hydrodynamic simulations of the mechanical effects of supernovae-driven superbubbles on the gas and metal content of dwarf galaxies, Mac Low & Ferrara (1998) have shown that moderate starburst events (SN II rates of $> 3 \text{ Myr}^{-1}$) in even massive dwarf galaxies ($10^9 M_{\odot}$) can blow out a substantial fraction ($\sim 70\%$) of metal-enriched gas without losing a significant amount of primordial gas ($< 0.001\%$). This process might be more important for SNe II, which are highly spatially and temporally correlated, than for SNe Ia, which seem to be relatively isolated in both time and position within a galaxy. This may enable low- σ galaxies to lose their SN II products preferentially without losing gas that can later be enriched by SNe Ia and recycled into new stars.

Although scenarios 5 and 6 predict similar abundance *trends* with σ , they appear to differ in their absolute abundance ratios. With “normal” yields, the early winds in scenario 6 would result in lower-than-normal abundances of Type II products in low- σ galaxies, but normal abundances in high- σ galaxies, where all products are retained. This is not as observed; $[E/Fe]$ is solar in low- σ galaxies and enhanced in high- σ galaxies (Figure 5). To work, scenario 6 may therefore have to be “tweaked” by a blanket upward adjustment of the Type II yield in *all* elliptical galaxies, designed to return $[E/Fe]$ in low- σ galaxies to the solar value. Such a tweak might be achieved, for example, by boosting the upper end of the IMF in all ellipticals by a similar amount. This requirement would constitute an additional burden on scenario 6.

In summary, there appear to be two viable scenarios that can currently account for all three observational trends with σ : (1) a flatter top end of the IMF that produces more massive stars at high σ , and (2) weaker early winds, less mass loss, and greater

³This is the place to clarify a potentially confusing aspect of our terminology. Earlier we stressed that high values of $[E/Fe]$ do not reflect an “enhancement” of the E elements but rather a depression of the Fe-peak elements, yet here scenario 5 accounts for high $[E/Fe]$ by “increasing” the effective yield of Type II elements. We seem to be saying simultaneously that the E elements are enhanced and not enhanced. Actually, these two statements are not in contradiction. The non-enhancement mentioned earlier refers to $[E/Z]$, which is always near zero since E effectively *is* Z. Scenario 5 deals on the other hand with $[E/Fe]$, which clearly *can* be increased by raising the absolute yield of Type II elements over Type Ia. The quantities $[E/Z]$ and the yield of the E elements are not the same, and one can be “enhanced” and not the other.

retention of SN II products at higher σ . Although we cannot tell which hypothesis is better, it is interesting, and a significant step forward, that the data seem to prefer scenarios in which it is the number or effectiveness of Type II SNe that are modulated, not the number of Type Ia's. A further new clue is that $[E/Fe]$ correlates most tightly with σ and not with other related structural parameters, such as mass or radius. This tells us that the processes modulating Type II SNe depend directly on the actual speeds of gas clouds, or possibly on the escape velocity from the galaxy. Finally, it is necessary to restate the disclaimer that to reach these firmer conclusions required using all three observational tests, including the two less universal correlations involving $[Z/H]$ and $[Fe/H]$. If these were thrown out, five out of the six scenarios would still be viable.

7. THE ORIGIN OF THE Z-PLANE

The origin of the Z-plane proves to be more telling and more difficult to explain than the $[E/Fe]$ - σ relation. Two basic star-formation scenarios for ellipticals are considered: (1) a pure single-burst population having the measured SSP age and composition, and (2) a double-burst population consisting of an old “base” population with a “frosting” of young stars. More complex scenarios can be inferred by extrapolating the results of the two-burst model.

7.1. Single-burst stellar populations and their evolution

Under the single-burst hypothesis, we observe that the Z-plane is in place at the present time (Figure 4) and ask how it evolved in the past and how it will evolve in the future. The evolution of the Z-plane under pure single-burst SSP populations is simple: galaxies move horizontally in t as they age but stay constant in both $[Z/H]$ and σ . Figure 10 shows this behavior. Note that since the ordinate is $\log t$ and not (linear) t , old objects move less per unit time today than young objects. Lines of constant σ therefore *steepen* into the future, and after enough time they actually curve upwards. This curvature becomes pronounced after 5 Gyr, as shown in Figure 10c. Similarly, lines of constant σ curve *downwards* in the past, as seen in Figure 10a. Under the single-burst hypothesis, we must therefore live at the special time when the $[Z/H]$ - t - σ surface is planar—i.e., lines of constant σ are straight only at the present time. This seems improbable.

There are two additional problems with the single-burst scenario. In the rather recent past, many young galaxies seen today would not exist at all if their populations really are pure SSPs. For example, 12 of 51 galaxies (24%) in the present sample would not have existed just 5 Gyrs ago (note how they have disappeared from Figure 10a). Second, if the monotonically rising age-metallicity relation at constant σ that is seen today is not special to this moment but will persist in future, the metallicities of newly formed young galaxies must be rising very rapidly at the present time. In a few Gyr from now, new populations will have to have metallicities in excess of $[Z/H] \sim +1$ (ten times solar)! Both of these problems illustrate again that the Z-plane is a short-lived, ephemeral phenomenon under the single-burst hypothesis, and that our present epoch would have to be very special.

7.2. Frosting models and their evolution

The second scenario is the simplest composite stellar population model, a double-starburst model in which a small “frosting” of young stars forms on top of an old, “base” population.

Examples of such models and their behavior are discussed in the Appendix. To a first approximation, SSPs add vectorially (when weighted by light) in the $H\beta$ - Mgb and $H\beta$ - $\langle Fe \rangle$ diagrams if the populations are not very far apart, but trajectories between widely separated populations are curved and must be calculated explicitly. We do this by computing light-weighted mean values of $H\beta$, Mgb , and $\langle Fe \rangle$, from which the SSP-equivalent parameters are computed using the formalism described in Paper I.

Four illustrative frosting models are shown in Figure 11 and Table 6. We begin by choosing two base populations (lower right) that would fall on the metallicity hyperplane at age 15 Gyr if they were pure SSPs, one at 250 km s^{-1} (the “giant” model) and one at 100 km s^{-1} (the “dwarf” model). At an age of 9.5 Gyr in each model, we turn on a frosting population of 20% by mass and allow the composite population to age for a further 5.5 Gyr after this burst, which we identify as the present time. Two frosting populations are employed, a solar-composition model with solar abundance ratios, and a metal-rich model with $[Z/H] = 0.5$ and $[E/Fe] = 0.25$. Each frosting is combined with each base, making four models in all.

The evolution of these populations is shown in Figure 11. Initially the composite populations jump to very young SSP-equivalent ages, moderate-to-high metallicities, and relatively high $[E/Fe]$ (long arrows to upper left of diagram). As the populations age, the SSP-equivalent ages become rapidly older while $[Z/H]$ and $[E/Fe]$ decrease. Finally, after several Gyr, the populations have drifted back close to their starting points, executing a large loop.

In order to match the data, this scenario must place galaxies back on the Z-plane at the present time. Since σ does not change in this simple model, this means that galaxies must come back to the correct σ contour, allowing for the fact that some galaxies of their type may not have suffered a star burst and thus continued to evolve passively to the right. These evolved points are shown by the large dots; their corresponding σ contours are the two grey bands, each $\pm 1\sigma_{[Z/H]}$ wide, where $\sigma_{[Z/H]}$ is the rms residual of $[Z/H]$ about the plane, i.e., 0.09 dex (Sec. 3.2). If a frosting galaxy winds up in the appropriate grey band after 5.5 Gyr, we will count it as lying in the Z-plane, and the model is a success.

Whether or not this will happen depends on a proper match between the metallicity of the base population and that of the frosting. The giant base ($[Z/H] = +0.1$) plus metal-rich frosting ($[Z/H] = +0.5$) is an example of a successful combination; it falls exactly in the middle of the allowed grey band at the present time (upper solid model). The same base enriched with a *solar*-metallicity frosting is less successful because the combination falls *below* the allowed grey band (upper dotted model). From these two models, it can be seen that the metal abundance of a successful frosting must be between 0.1 and 0.6 dex more metal rich than the giant base population to which it is added. Similar reasoning implies that the same window—0.1–0.6 dex more metal rich—applies to dwarf bases, too.

The width of these windows depends on the age of the starburst. Turning on the starburst 5.5 Gyr ago was arbitrary and resulted in fairly red, old-looking models at the present time. Since many SSPs are observed to be quite young, matching them requires more recent starbursts. Metallicity constraints then get tighter—it may be shown that the allowed $[Z/H]$ window shrinks in width and the frosting population must be considerably *more* metal-rich than the base.

Apparent $[E/Fe]$ values must also stay constant during this

TABLE 6
EVOLUTION OF TWO-BURST FROSTING MODELS

Model ^a	t	Base		t	Frosting		$H\beta$	Mgb	Composite			
		[Z/H]	[E/Fe]		[Z/H]	[E/Fe]			$\langle Fe \rangle$	t	[Z/H]	[E/Fe]
GS	10.0	0.10	0.21	0.5	0.00	0.00	4.19	2.66	2.07	0.7	0.23	0.26
	10.5			1.0			2.67	3.64	2.50	1.2	0.25	0.22
	11.0			1.5			2.13	4.16	2.65	2.0	0.14	0.15
	11.5			2.0			1.86	4.49	2.77	3.3	0.13	0.13
	12.0			2.5			1.77	4.61	2.81	4.5	0.12	0.13
	13.0			3.5			1.65	4.76	2.85	6.9	0.09	0.13
	14.0			4.5			1.57	4.90	2.90	8.2	0.07	0.13
	15.0			5.5			1.51	5.00	2.93	9.7	0.07	0.14
DS	10.0	-0.22	0.08	0.5	0.00	0.00	4.13	2.40	1.98	0.7	0.20	0.17
	10.5			1.0			2.69	3.20	2.36	1.5	-0.03	0.11
	11.0			1.5			2.20	3.59	2.48	2.7	-0.07	0.07
	11.5			2.0			1.96	3.86	2.59	4.3	-0.06	0.06
	12.0			2.5			1.88	3.93	2.62	5.3	-0.06	0.06
	13.0			3.5			1.77	4.02	2.65	7.6	-0.10	0.05
	14.0			4.5			1.70	4.11	2.68	9.4	-0.13	0.05
	15.0			5.5			1.64	4.19	2.71	10.7	-0.14	0.05
GR	10.0	0.10	0.21	0.5	0.50	0.25	5.04	1.92	1.55	0.7	0.59	0.40
	10.5			1.0			3.44	2.81	2.13	1.6	0.41	0.25
	11.0			1.5			2.60	3.31	2.43	2.8	0.32	0.24
	11.5			2.0			2.21	3.62	2.58	4.8	0.25	0.22
	12.0			2.5			2.06	3.78	2.64	5.7	0.25	0.22
	13.0			3.5			1.87	4.00	2.70	7.8	0.23	0.21
	14.0			4.5			1.78	4.14	2.73	9.2	0.23	0.22
	15.0			5.5			1.69	4.26	2.76	10.4	0.23	0.22
DR	10.0	-0.22	0.08	0.5	0.50	0.25	4.95	1.75	1.50	0.8	0.41	0.27
	10.5			1.0			3.42	2.51	2.03	1.9	0.13	0.15
	11.0			1.5			2.62	2.92	2.31	4.0	0.05	0.15
	11.5			2.0			2.27	3.18	2.44	6.5	0.04	0.14
	12.0			2.5			2.13	3.30	2.49	7.6	0.01	0.13
	13.0			3.5			1.96	3.46	2.54	9.5	-0.01	0.12
	14.0			4.5			1.87	3.54	2.55	11.1	-0.02	0.12
	15.0			5.5			1.79	3.62	2.57	12.1	-0.02	0.12

^a“G” is the giant elliptical base model ($\sigma = 250 \text{ km s}^{-1}$); “D” is the dwarf elliptical base model ($\sigma = 100 \text{ km s}^{-1}$); “S” is the solar metallicity, solar enhancement ratio frosting; “R” is the metal-rich, super-solar enhancement ratio frosting. All frostings represent 20% of total mass. See text and Figure 11 for details.

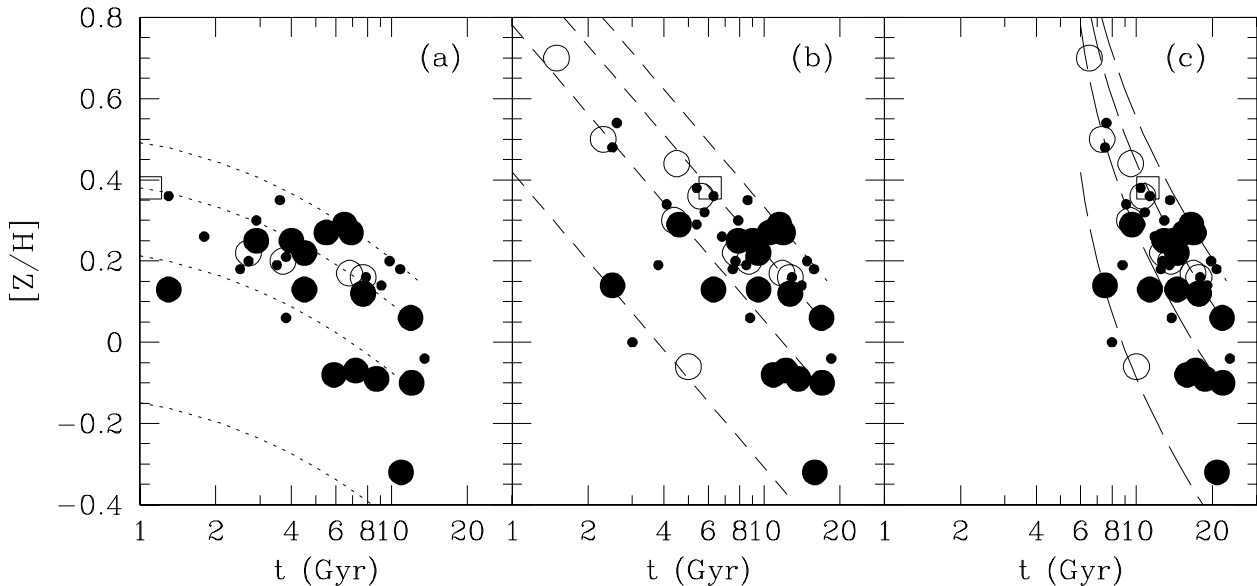


FIG. 10.— The time evolution of galaxies in the Z-plane for pure SSPs. Points are coded by environment (see Figure 7). Lines are loci of constant velocity dispersion: from bottom to top, $\sigma_0 = 50, 150, 250, 350 \text{ km s}^{-1}$ (see Figure 4). (a) The metallicity hyperplane 5 Gyr ago. (b) The metallicity hyperplane today. (c) The metallicity hyperplane 5 Gyr from now. Note the strong curvature in lines of constant σ in panels (a) and (c).

process, since by hypothesis σ is assumed not to change (Eq. 9; Fig. 5). This further requires that $[E/Fe]$ for the frosting population be nearly equal to that of the base population, as composite SSP enhancement ratio is close to the mean of the frosting and base populations at moderate burst strength (this point was also made by Jørgensen 1999).

The close coordination required for both $[Z/H]$ and $[E/Fe]$ in frosting models may place tight constraints on star formation scenarios for elliptical galaxies. In particular, it seems hard to meet the necessary tight limits on $[Z/H]$ and $[E/Fe]$ if young populations form from unrelated, “foreign” gas acquired in a merger. Such coordination would seem more natural if the frosting gas were pre-enriched *within the parent galaxy itself*. An example of such a model might be low-mass star formation in gas re-accreted in a galactic cooling flow (Mathews & Brighenti 1999).

Several questions remain about the frosting scenario:

(1) The frosting model as presented here consists of only two bursts. More realistic scenarios would contain extended star formation over time.

(2) Some of the most extreme young populations in the present sample are clearly in disturbed galaxies: NGC 6702 (Davoust et al. 1987; Tonry et al., priv. comm.), NGC 1700, NGC 584, and NGC 5831 (Schweizer & Seitzer 1992), which are excellent candidates for recent star formation in mergers. We have argued that such star formation would likely disobey the hyperplane, yet these objects fall nicely on it (Figures 2, 4). Their agreement with the hyperplane suggests that the previous argument against foreign gas captured in mergers may not be fully correct.

(3) The stellar population parameters considered here are only central values ($r_e/8$). The global stellar populations ($r_e/2$) are generally older by $\sim 25\%$ and more metal-poor by -0.20 dex, while $[E/Fe]$ is basically the same (Paper I). We believe that global populations also obey a hyperplane but have not yet examined it in detail. Radial gradients and global stellar popu-

lations will be discussed in a future paper.

8. CONCLUSIONS

The centers of local elliptical galaxies appear to contain quite complex stellar populations. The present sample of local ellipticals spans a wide range of stellar population parameters, most notably a large range in SSP-equivalent age (especially in, but not limited to, field ellipticals).

Despite their diversity, the central stellar populations of these galaxies are described by a few simple scaling relations. (1) Abundance parameters $[Z/H]$ and $[E/Fe]$ are specified to high accuracy by SSP-equivalent age, t , and central velocity dispersion σ ; ellipticals thus occupy a “metallicity hyperplane” in $([Z/H], \log t, \log \sigma, [E/Fe])$ -space. (2) SSP-equivalent metallicity, $[Z/H]$, is a function of both t and σ (the “Z-plane”). At fixed t , $[Z/H]$ increases with σ ; at fixed σ , $[Z/H]$ is larger at younger age. (3) SSP-equivalent enhancement ratio, $[E/Fe]$, is found to be a monotonically increasing function of σ only, in the sense that adding other structural parameters such as I_e or r_e does not predict either $[E/Fe]$ or $[Z/H]$ more accurately.

Our use of SSP-equivalent parameters is not meant to imply a single-burst origin for elliptical galaxies; in fact, the existence of the Z-plane seems to imply that the populations are largely old with a “frosting” extending to younger ages. However, despite the fact that SSP-parameters are not true means but rather likely to be influenced by the light of younger stars, they still place very important constraints on the history of star formation in elliptical galaxies (see below).

We take σ and t as the independent parameters that specify the distribution of galaxies in the hyperplane. Any variation in this distribution will influence all other two-dimensional projections of SSP parameters, and thus many of the common scaling laws for elliptical galaxies. Our sample shows a possible difference in the (σ, t) distribution with environment—our field ellipticals span a wide range in SSP age, while the Fornax and Virgo ellipticals are generally old. This results in a signif-

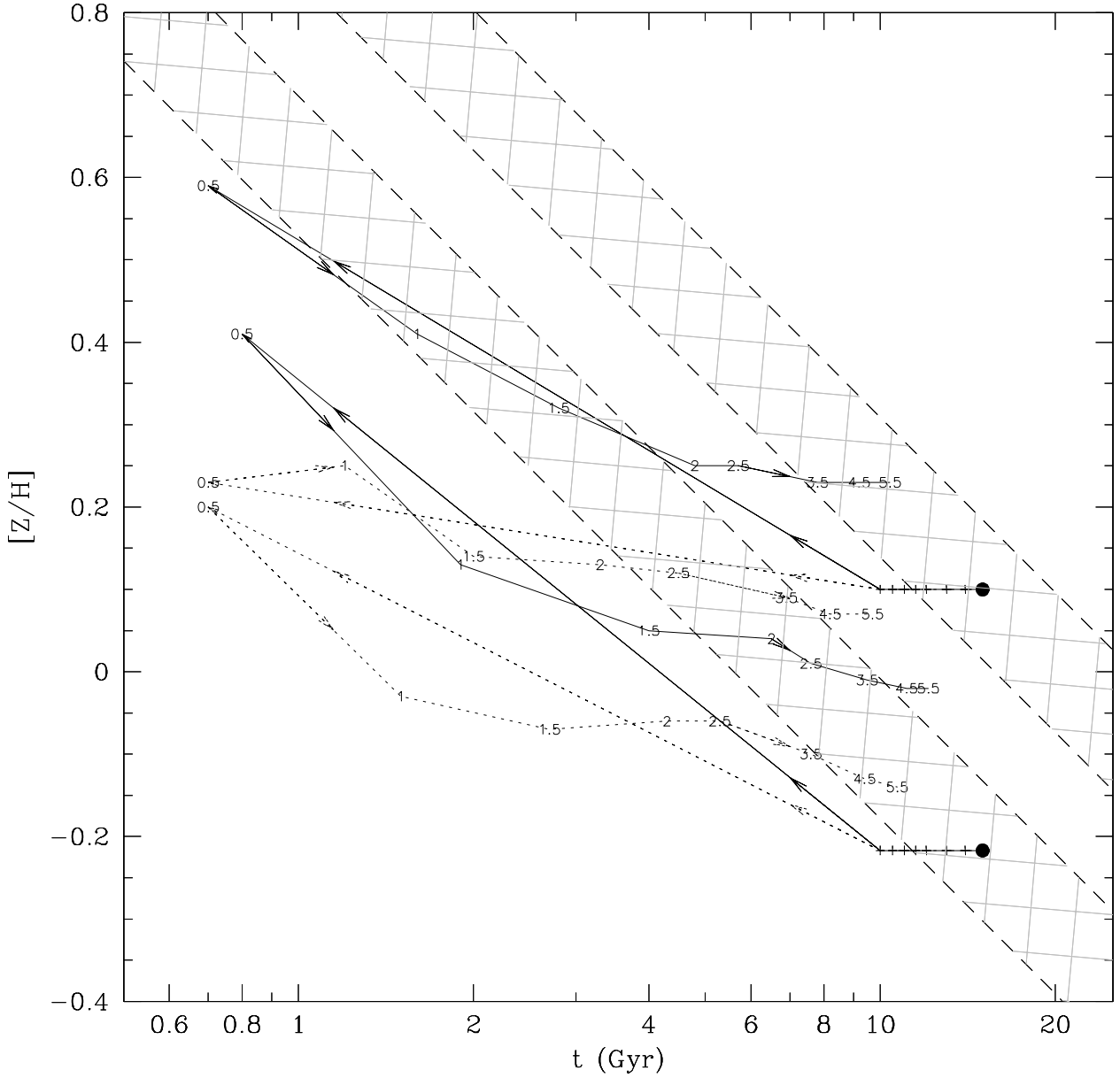


FIG. 11.— The time evolution of frosting models in the $(t, [Z/H])$ projection of the Z-plane. Two base models are shown: a “giant” elliptical base population ($\sigma = 250 \text{ km s}^{-1}$, $[Z/H]_{\text{base}} = 0.10$ dex, and $[E/Fe]_{\text{base}} = 0.22$ dex) and a “dwarf” elliptical base population ($\sigma = 100 \text{ km s}^{-1}$, $[Z/H]_{\text{base}} = -0.22$ dex, and $[E/Fe]_{\text{base}} = 0.08$ dex); $[Z/H]$ and $[E/Fe]$ were chosen to place the base populations on the present-day metallicity hyperplane at $t = 15$ Gyr (large filled circles). SSP-equivalent populations that today lie in the gray-hatched bands should have the same σ as the base population to lie in the observed Z-plane (the width of the bands is the typical $\pm 1\sigma$ uncertainty in $[Z/H]$). Two frosting populations are shown for each base population: a solar-metallicity frosting ($[Z/H]_{\text{frost}} = 0.0$ dex and $[E/Fe]_{\text{frost}} = 0.0$ dex; dotted trajectories) and a metal-rich frosting ($[Z/H]_{\text{frost}} = 0.50$ dex, $[E/Fe]_{\text{frost}} = 0.25$ dex; solid trajectories). Each frosting is 20% by mass of the total population and turns on at 9.5 Gyr. The bursts are allowed to age for 5.5 Gyr until a final age of the base population of 15 Gyr. The crosses represent the passive evolution of the base population as seen at 10, 10.5, 11, 11.5, 12, 13, 14, and 15 Gyr. The composite population is marked with a number representing the time in Gyr after the starburst of the frosting population. (Frosting populations at 0.5 Gyr were generated from the Padua models of Appendix A of Paper I, for which line strengths are available down to 0.4 Gyr.) After aging for $\sim 3\text{--}5$ Gyr, the composite populations successfully pass through the same band of constant σ as the base population (but at higher SSP metallicity and younger SSP age) only if $[Z/H]_{\text{frost}}$ exceeds $[Z/H]_{\text{base}}$ by 0.1 to 0.6 dex and $[E/Fe]_{\text{frost}} \sim [E/Fe]_{\text{base}}$.

icant mass-metallicity trend for the cluster galaxies but not for the field galaxies. Other correlations between stellar population parameters and structural parameters may also turn out to vary with environment.

The $Mg-\sigma$ relations are edge-on projections of the metallicity hyperplane. At a given σ , young age is offset by a correspondingly high metallicity, preserving line strength. The narrowness of the observed $Mg-\sigma$ relations therefore does not imply a narrow range of ages at fixed velocity dispersion. A more detailed look at the $Mg-\sigma$ relations is the subject of a future paper.

Physical models to account for the hyperplane have been considered. The rise in $[E/Fe]$ with σ and the mass-metallicity relation (at fixed t) is consistent with a higher effective yield of Type II SNe products at high σ . This trend has several possible explanations, for example, greater retention of outflow-driven gas or a flatter IMF at high σ .

The existence of the Z-plane is more challenging. A “frosting” scenario is favored, in which young stars are added to an old base population, resulting in a range of SSP-equivalent ages. With a suitable choice of burst populations, the composite populations can be engineered to lie on lines of constant σ in the Z-plane after a few Gyr. However, to preserve both the Z-plane and the $[E/Fe]-\sigma$ relation requires that abundances in the frosting population must be closely coupled to that of the base population—the metallicity, $[Z/H]$, of the frosting must be somewhat higher than that of the base population, while the enhancement ratio, $[E/Fe]$, must be nearly equal. The frosting scenario therefore seems to favor star formation from gas that was pre-enriched in the same parent galaxy rather than from gas that was accreted in an unrelated merger. However, several merger remnants in the sample do indeed lie nicely on the Z-plane, in defiance of this logic.

The present picture of the hyperplane is preliminary and needs to be checked against a better local sample and a wide array of other data. For example, SSP mass-to-light ratios should be compared to dynamical M/L measurements, and *global* SSP parameters should be analyzed, as they are more indicative of the global star formation history than the central SSP parameters used here. A further interesting question is whether the

color-magnitude relation and other scaling laws might also be near-edge-on projections of the hyperplane, like $Mg-\sigma$.

Most important, the implications of the frosting model must be developed for lookback observations of distant elliptical galaxies. Many observations of distant cluster ellipticals suggest that their stellar populations formed very early, and this may be consistent with the generally old ages for cluster galaxies found here. Our field ellipticals do show a wide spread of SSP ages, but we have noted that the sample is not volume-limited, and thus predictions for the evolution of distant field ellipticals cannot yet be drawn. In short, a great deal more data must be gathered and reconciled before we can claim a solid understanding of the star formation histories of elliptical galaxies.

It is a pleasure to thank a great number of our colleagues for interesting discussions. Drs. R. Bender, M. Bolte, D. Burstein, R. Carlberg, J. Dalcanton, R. Davies, A. Dressler, R. Ellis, W. Freedman, G. Illingworth, D. Kelson, I. King, R. Marzke, W. Mathews, A. McWilliam, J. Mould, J. Mulchaey, A. Oemler, A. Renzini, M. Rich, P. Schechter, F. Schweizer, T. Smecker-Hane, P. Stetson, S. Yi, and A. Zabludoff have all provided hours of stimulating conversations. We are indebted to Dr. M. Tripicco for sending us electronic versions of his and Dr. Bell’s results on the response of the Lick/IDS indices to abundance variations, to Dr. H. Kuntschner for providing his data on Fornax early-type galaxies in advance of publication, to Dr. D. Kelson for plane-fitting software, and to Drs. J. Tonry, J. Blakeslee, and A. Dressler for providing SBF distances to local ellipticals in advance of publication and for allowing S. C. T. to examine their images of NGC 6702. The comments of an anonymous referee helped greatly to improve the presentation. Support for this work was provided by NASA through Hubble Fellowship grant HF-01125.01-99A to SCT awarded by the Space Telescope Science Institute, which is operated by the Association of Universities for Research in Astronomy, Inc., for NASA under contract NAS 5-26555, by a Starr Fellowship to SCT, by a Flintridge Foundation Fellowship to SCT, and by NSF grant AST-9529098 to SMF.

APPENDIX

MODELS OF COMPOSITE STELLAR POPULATIONS

In this section we discuss simple models of composite stellar populations based on double bursts. Our approach is similar to the “isochrone synthesis” method of Bruzual & Charlot (1993), in which composite populations are built up from single stellar populations (SSPs) treated as δ -functions.

At present, it is not our intent to create grids of models with multiple populations drawn from galaxy formation and evolution models including the effects of winds, blowout, and other processes (see Arimoto & Yoshii 1987 and Tantalo et al. 1998b for two examples of this approach). Rather, we are interested in determining rough rules of thumb for adding multiple populations in the $H\beta$ -metallicity diagrams. Specifically we ask how mixtures of two bursts or multiple metallicities combine to mimic a single SSP of a given age and metallicity.

We begin by describing the method used to combine the W94 SSPs to derive line strengths. We then discuss two models of composite populations: galaxies with multiple (here, two) bursts of star formation, and a model with a single age but a dispersion in metallicity based on the metallicity spread of M32 as determined by Grillmair et al. (1996). We show that line strengths add as vectors in the diagrams to first order (when weighted by light). There is thus an infinite number of ways of decomposing a given population into single-burst components. Determining the detailed star formation histories of old stellar populations from the present data is highly underconstrained.

Method

The line strength for a single stellar population (when expressed as an equivalent width in Å) can be written

$$EW = w \left(1 - \frac{F_l}{F_C} \right), \quad (\text{A1})$$

where w is the width of the feature bandpass in Å, F_l is the observed flux (per unit mass) integrated over the feature bandpass, and F_C represents the observed flux (per unit mass) of the straight line connecting the midpoints of the blue and red pseudocontinuum levels, integrated over the feature bandpass (Worthey et al. 1994; Trager et al. 1998; Paper I). In a composite population, the fluxes become sums over populations and therefore

$$EW = w \left(1 - \frac{\sum_i f_i F_{l,i}}{\sum_i f_i F_{C,i}} \right), \quad (\text{A2})$$

where i represents each individual population, f_i is the fraction by mass of each population ($\sum_i f_i = 1$), and $F_{l,i}$ and $F_{C,i}$ are the integrated fluxes in the feature bandpass and in the “continuum” of each population i .

We assume that $F_{C,i}$ is independent of $[E/Fe] \neq 0$, which is consistent with the tracks of Salaris & Weiss (1998), in which the turnoff and RGB move horizontally but do not change luminosity. For each population we can then write

$$F_{l,i} = F_{C,i} \left(1 - \frac{I_i(t, [Z/H], [E/Fe])}{w} \right), \quad (\text{A3})$$

where $I_i(t, [Z/H], [E/Fe])$ is the line strength of population i for the index in question at age t , metallicity $[Z/H]$, and enhancement ratio $[E/Fe]$. The model values $F_{l,i}$ and $F_{C,i}$ values are then inserted into Equation A2 to determine the line strength of the composite population for each index of interest.

Models

Double starbursts

Three double-starburst models are developed, chosen illustratively such that their composite line strengths cover the observed loci of the G93 galaxies. Model A covers giant ellipticals with $\sigma \gtrsim 200 \text{ km s}^{-1}$; its old component has $(t, [Z/H], [E/Fe]) = (17 \text{ Gyr}, +0.15, +0.25)$, similar to the oldest galaxies in the sample, mixed with a young burst having parameters $(1 \text{ Gyr}, +0.75, 0.0)$. Model B covers small ellipticals with $\sigma \lesssim 200 \text{ km s}^{-1}$. Its old population has $(17 \text{ Gyr}, -0.25, 0.0)$, mixed with a young population of $(1 \text{ Gyr}, +0.5, 0.0)$. Model C is an alternative to model B in which metal-enriched winds are imagined to selectively blow out SN II products but not those from SN Ia (Mac Low & Ferrara 1999). Its old population has $(17 \text{ Gyr}, -0.25, +0.25)$, and its young burst has $(1 \text{ Gyr}, +0.5, -0.25)$ (highly enriched in SN Ia products). In all models, the young burst is allowed to vary in strength from 10%–100% of the final mass.

The models are summarized in Table A1 and illustrated in Figure A1, which shows the weights expressed as percentage of *mass*, and in Figure A2, which shows the weights expressed as percentage of *light*. The latter figure demonstrates the useful rule of thumb that composite, two-burst populations add roughly as light-weighted vectors in the Balmer–metal line strength diagrams. This is shown by the relatively straight lines linking the endpoint populations in Figure A2 and the relatively uniform tickmark spacing along the lines. Taking model C as an example, we can compare the light-weighted vector rule for predicting the 50/50 population, versus its actual location in the diagrams. For model C, the real composite 50/50 population (50% old, 50% young by light) is at $(1.9 \text{ Gyr}, +0.23, +0.02)$ while the vector-added point midway between the two endpoints is at $(2.5 \text{ Gyr}, 0.0, -0.05)$. For an 80/20 model (80% old, 20% young by light), the real population is at $(7.3 \text{ Gyr}, -0.04, +0.15)$ compared to the vector-added population at $(9.5$

TABLE A1
TWO-BURST COMPOSITE STELLAR POPULATION MODELS

Model	t	Base			Frosting				Composite							
		$[Z/H]$	$[E/Fe]$	M/L_V	t	$[Z/H]$	$[E/Fe]$	M/L_V	f_M^a	f_L^b	$H\beta$	Mgb	$\langle Fe \rangle$	t	$[Z/H]$	$[E/Fe]$
A	17	+0.15	+0.25	10.0	1	+0.75	0.00	1.3	0.10	0.46	2.12	4.08	2.88	2.2	+0.50	+0.15
									0.12	0.50	2.19	3.98	3.01	2.0	+0.49	+0.13
									0.40	0.84	2.73	3.22	3.12	1.3	+0.69	+0.03
B	17	−0.25	0.00	7.9	1	+0.50	0.00	1.2	0.10	0.42	2.35	3.16	2.67	2.8	+0.08	0.00
									0.14	0.50	2.50	3.07	2.67	2.1	+0.15	0.00
									0.40	0.81	3.05	2.74	2.70	1.3	+0.38	0.00
C	17	−0.25	+0.25	7.9	1	+0.50	−0.25	1.2	0.10	0.42	2.33	3.35	2.65	2.7	+0.14	+0.06
									0.14	0.50	2.48	3.18	2.72	1.9	+0.23	+0.02
									0.40	0.81	3.00	2.57	2.99	1.3	+0.42	−0.14

^aFractional mass of burst

^bFraction of V-band light in burst

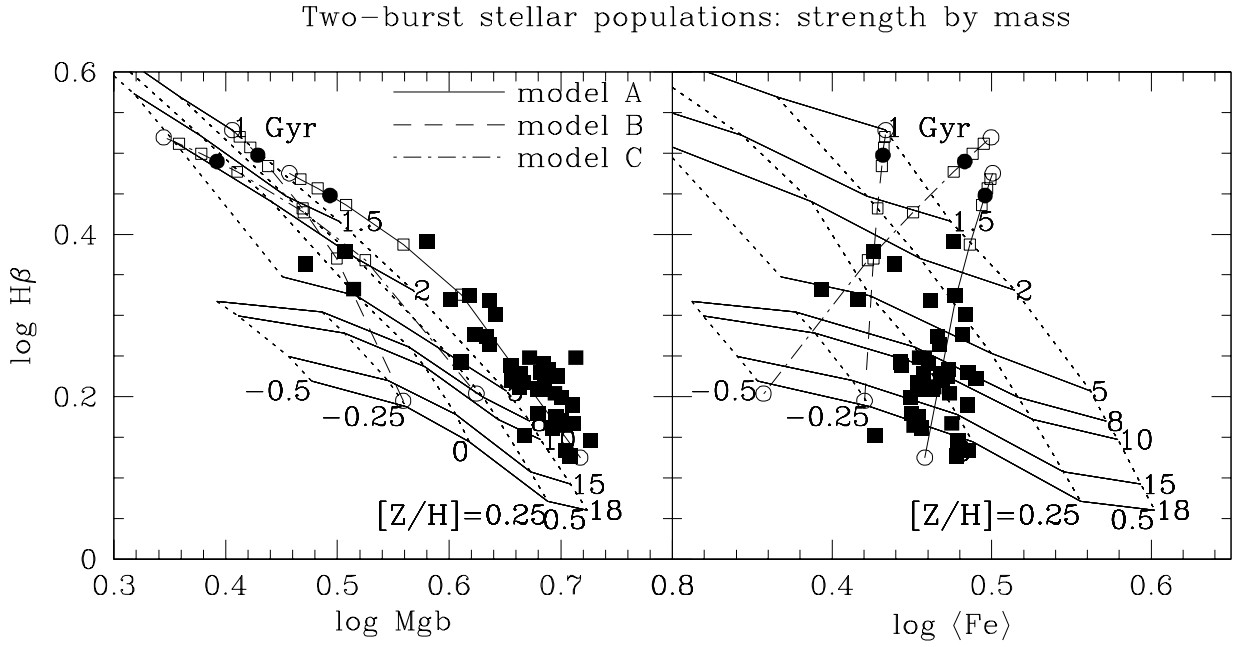


FIG. A1.— Schematic two-burst models. Three models are shown: (A) a 17 Gyr, $[Z/H] = +0.15$ dex, $[E/Fe] = +0.25$ dex progenitor (typical of the oldest giant ellipticals in the sample) with a 1 Gyr, $[Z/H] = +0.75$ dex, solar-neighborhood abundance ratio burst, meant to cover the stellar populations of the high- σ galaxies (solid line); (B) a 17 Gyr, $[Z/H] = -0.25$ dex, solar-neighborhood abundance ratio progenitor with a 1 Gyr, $[Z/H] = +0.5$ dex, solar-neighborhood abundance ratio burst, meant to cover the stellar populations of the low- σ galaxies NGC 221 (M32), NGC 4489, and NGC 7454 (short-dashed line); and (C) a 17 Gyr, $[Z/H] = -0.25$ dex, $[E/Fe] = +0.25$ dex progenitor with a 1 Gyr, $[Z/H] = +0.5$ dex, $[E/Fe] = -0.25$ dex burst, meant to represent possible star formation after a metal-enriched wind in a low- σ galaxy (dot-dashed line). Bursts of 10%, 20%, 40%, 60%, and 80% (open squares) and 50% (solid circles) by mass are shown. Open circles represent the progenitor (lower) and burst (upper) populations. Solid squares are the G93 galaxies; compare to Figure 1.

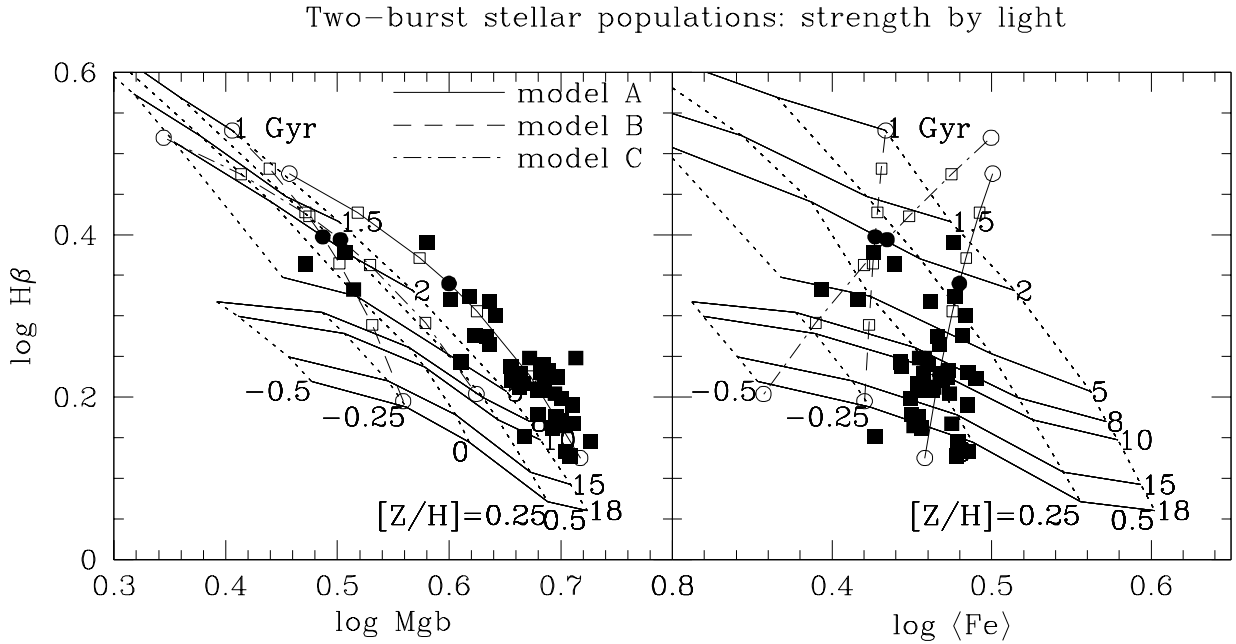


FIG. A2.— The same two-burst models as in Figure A1, but with burst strength now indicated by light fraction. Open symbols represent the fractional V-band luminosity of the young population: from bottom to top, 0%, 20%, 40%, 60%, 80% and 100%. These correspond to average mass fractions of 0%, 3%, 8%, 16%, 35%, and 100% for model A and 0%, 4%, 9%, 19%, 38%, and 100% for models B and C. The solid circles represent the 50% by light in young/old models, which correspond to 12% by mass in the young population for model A and 14% by mass in the young population for models B and C. The relative straightness of the lines and even spacing of the squares compared to Figure A1 indicate that stellar populations add roughly as light-weighted vectors in these diagrams.

Gyr, -0.15 , $+0.15$). Thus, vector weighting by light tends to overestimate the age by about 25%, underestimate $[Z/H]$ by 0.1 – 0.25 , and underestimate $[E/Fe]$ by less than about 0.1 . These are extreme cases, and the errors for mixing two populations closer in the diagrams would be smaller.

In the past, we have stated that the best-fitting SSP-equivalent age (as derived here) is close to the “light-weighted” age (Faber et al. 1995). This was a mis-statement. The light-weighted age of the 50/50 model is simply the average of 1 Gyr and 17 Gyr, or 9 Gyr, much larger than the SSP-equivalent age, of 1.8 Gyr. What we meant to say is that composite populations add in the diagrams like *light-weighted vectors*. As noted, the age agreement is much better, within 50%, when computed this way. However, valuable as such rules of thumb may be for cultivating intuition, the only proper way to compare models to data is to add up the fractional index contributions using Equation A2.

The light-weighted vector rule cannot be taken too far and does better for $\langle Fe \rangle$ than for Mgb , whose trajectories are not as straight in the grid diagrams. This may prove to be a boon in accounting for the very high Mgb strengths of galaxies like NGC 507, NGC 6702, and NGC 720, whose Mgb indices lie high up and to the right in Figure 1. Such populations might be modeled as recent starbursts, as suggested independently by their high morphological disturbance parameters (Faber et al. 1995).

Metallicity spreads

Yet a fourth model (not shown) explores the effect of a spread in metallicities at a single age. This model is based on the metallicity distribution in an outer field of M32 determined by Grillmair et al. (1996; their Figure 10), which has a strong peak at $[Fe/H] = [Z/H] = -0.20$, FWHM of about 0.5, a weak tail to low metallicities down to -1.2 , and a light-weighted mean metallicity of -0.25 (note that $[E/Fe] \approx 0.00$ for M32). For an assumed single age of 8.5 Gyr, the composite model yields $H\beta = 2.02 \text{ \AA}$, $Mgb = 2.89 \text{ \AA}$, and $\langle Fe \rangle = 2.29 \text{ \AA}$, in good agreement with the outwardly extrapolated data from G93 of $H\beta = 1.92 \text{ \AA}$, $Mgb = 2.99 \text{ \AA}$, and $\langle Fe \rangle = 2.42 \text{ \AA}$ (Grillmair et al. 1996).

The SSP-equivalent stellar population parameters of the composite model are $t = 8.2$ Gyr, $[Z/H] = -0.32$, and $[E/Fe] = 0.00$. These results show that the integrated light from a uniform-age population with a strongly peaked metallicity distribution resembles a population of nearly the same age (or slightly younger if metal-poor stars are present) and of very similar $[Z/H]$ to the true light-weighted metallicity ($[Z/H] = -0.25$). These results agree with composite multi-metallicity populations by Greggio (1997), who found that shifts of SSP-equivalent metallicities in mixed-metallicity populations were not large in the absence of large metal-poor tails.

To summarize, the results in this Appendix suggest that metallicity spreads (and, by extension, spreads in $[E/Fe]$) at fixed age do not seriously skew the indices, but that even small populations of recently-formed (within ~ 1 Gyr) stars can significantly reduce the inferred age. A burst of only 10% by mass 1 Gyr ago on top of a 17 Gyr old population gives an SSP-equivalent age of only ≈ 1.8 Gyr. Because line strengths add as vectors (weighted by the luminosity of each population), the ages and metallicities of each burst in a composite population are not separable using the present data.

REFERENCES

- Aaronson, M. & Mould, J. 1985, *ApJ*, 290, 191
 Arimoto, N. & Yoshii, Y. 1987, *A&A*, 173, 23
 Baade, W. 1963, *Evolution of Stars and Galaxies*, ed. C. Payne-Gaposchkin (Cambridge: Harvard University Press), p. 208
 Baum, W. A. 1959, *PASP*, 71, 106
 Bender, R. 1988, *A&A*, 193, L7
 Bender, R., Burstein, D., & Faber, S. M. 1992, *ApJ*, 399, 462
 Bender, R., Burstein, D., & Faber, S. M. 1993, *ApJ*, 411, 153
 Bender, R., Ziegler, B., & Bruzual, G. 1996, *ApJ*, 463, L51
 Bernardi, M., et al. 1998, *ApJ*, 508, L143
 Bower, R. G., Lucey, J. R., & Ellis, R. S. 1992, *MNRAS*, 254, 601
 Blumenthal, G. R., Faber, S. M., Primack, J. R., & Rees, M. J. 1984, *Nature*, 311, 517
 Bruzual A., G. & Charlot, S. 1993, *ApJ*, 405, 538
 Burstein, D., Faber, S. M., Gaskell, C. M., & Krumm, N. 1984, *ApJ*, 287, 586
 Burstein, D., Faber, S. M., & Dressler, A. 1990, *ApJ*, 354, 18
 Caon, N., Capaccioli, M., & D’Onofrio, M. 1994, *A&AS*, 106, 242
 Davies, R. L. 1996, in *New Light on Galaxy Evolution*, IAU Symp. 171, ed. R. Bender & R. L. Davies (Kluwer: Dordrecht), p. 37
 Davis, M. & Faber, S. M. 1998, in 14th IAP Colloquium, *Wide Field Surveys in Cosmology*, ed. S. Colombi & Y. Mellier (Gif-sur-Yvette: Editions Frontieres), in press
 Davoust, E., Capaccioli, M., Lelievre, G., & Nieto, J.-L. 1987, in *Structure and Dynamics of Elliptical Galaxies*, IAU Symposium 127, ed. T. de Zeeuw (Dordrecht: Kluwer), p. 407
 de Carvalho, R. R. & Djorgovski, S. 1992, *ApJ*, 389, L49
 de Vaucouleurs, G., de Vaucouleurs, A., Corwin, H. G., Buta, R. J., Paturel, G., & Fouque, P. 1991, *Third Reference Catalogue of Bright Galaxies* (New York: Springer-Verlag) (RC3)
 Dressler, A., Lynden-Bell, D., Burstein, D., Davies, R. L., Faber, S. M., Terlevich, R. J., & Wegner, G. 1987, *ApJ*, 313, 42
 Eggen, O. J., Lynden-Bell, D., & Sandage, A. R. 1962, *ApJ*, 136, 748
 Faber, S. M. 1973, *ApJ*, 179, 731
 Faber, S. M. 1977, in *The Evolution of Galaxies and Stellar Populations*, ed. B. M. Tinsley & R. B. Larson (New Haven: Yale University Observatory), p. 157
 Faber, S. M. & Jackson, R. E. 1976, *ApJ*, 204, 668
 Faber, S. M., Wegner, G., Burstein, D., Davies, R. L., Dressler, A., Lynden-Bell, D., & Terlevich, R. J. 1989, *ApJS*, 69, 763
 Faber, S. M., Worthey, G. & Gonzalez, J. J. 1992, in *The Stellar Populations of Galaxies*, IAU Symposium 149, ed. B. Barbuy & A. Renzini (Dordrecht: Kluwer), p. 255
 Faber, S. M., Trager, S. C., González, J. J., & Worthey, G. 1995, in *IAU Symposium 164, Stellar Populations*, ed. P. C. van der Kruit & G. Gilmore (Dordrecht: Kluwer), p. 249
 Faber, S. M., et al. 1997, *AJ*, 114, 1771
 Fisher, D., Franx, M., & Illingworth, G. 1995, *ApJ*, 448, 119
 Franx, M., Illingworth, G., & Heckman, T. 1989, *AJ*, 98, 538
 González, J. J. 1993, Ph.D. Thesis, University of California, Santa Cruz (G93)
 Goudfrooij, P., Hansen, L., Jorgensen, H. E., Norgaard-Nielsen, H. U., De Jong, T., & Van Den Hoek, L. B. 1994, *A&AS*, 104, 179
 Greggio, L. 1997, *MNRAS*, 285, 151
 Grevesse, N., Noels, A., & Sauval, A. J. 1996, in *Cosmic Abundances*, eds. S. S. Holt & G. Sonneborn, A.S.P. Conf. Ser., vol. 99 (San Francisco: ASP), p. 117
 Grillmair, C. J., et al. 1996, *AJ*, 112, 1975
 Gúzman, R., Lucey, J. R., Carter, D. & Terlevich, R. J. 1992, *MNRAS*, 257, 187
 Ho, L. C., Filippenko, A. V., & Sargent, W. L. W. 1997, *ApJS*, 112, 315
 Jørgensen, I. 1999, *MNRAS*, 306, 607
 Jørgensen, I., Franx, M., & Kjaergaard, P. 1996, *MNRAS*, 280, 167
 Kauffmann, G., White, S.D.M., & Guiderdoni, B. 1993, *MNRAS*, 264, 201
 Kuntschner, H. 1998, Ph.D. Thesis, University of Durham (K98)
 Kuntschner, H. & Davies, R. L. 1998, *MNRAS*, 295, L29
 Larson, R. B. 1974, *MNRAS*, 169, 229
 Larson, R. B., Tinsley, B. M., & Caldwell, C. N. 1980, *ApJ*, 237, 692
 Lee, Y.-W. 1994, *ApJ*, 430, 113
 Mac Low, M.-M. & Ferrara, A. 1999, *ApJ*, 513, 142
 Mathews, W. G. & Baker, J. C. 1971, *ApJ*, 170, 241
 Mathews, W. G. & Brighenti, F. 1999, *ApJ*, 527, 31
 O’Connell, R. W. 1976, *ApJ*, 206, 370
 Peletier, R. 1989, Ph.D. Thesis, Rijksuniversiteit Groningen

- Peletier, R. F., Davies, R. L., Davis, L. E., Illingworth, G. D., & Cawson, M. 1990, *AJ*, 100, 1091
- Peletier, R. F., Valentijn, E. A., & Jameson, R. F. 1990, *A&A*, 233, 62
- Pickles, A. J. 1985, *ApJ*, 296, 340
- Poulain, P. 1988, *A&AS*, 72, 215
- Poulain, P. & Nieto, J.-L. 1994, *A&AS*, 103, 573
- Prugniel, P. & Simien, F. 1996, *A&A*, 309, 749
- Renzini, A. 1995, in *Stellar Populations*, IAU Symp. 164, ed. P. C. van der Kruit & G. Gilmore (Dordrecht: Kluwer), p. 325
- Renzini, A. 1998, in *The Young Universe*, ed. S. D'Odorico, A. Fontana, & E. Giallongo, ASP Conf. Ser., vol. 146, p. 298
- Salaris, M. & Weiss, A. 1998, *A&A*, 335, 943
- Sandage, A. 1972, *ApJ*, 176, 21
- Sandage, A. & Visvanathan, N. 1978, *ApJ*, 225, 742
- Sandage, A. & Tammann, G. A. 1987, *A Revised Shapley-Ames Catalog of Bright Galaxies*, 2nd ed. (Washington, D. C.: Carnegie Institution of Washington) (RSA)
- Sandage, A. & Bedke, J. 1994, *The Carnegie Atlas of Galaxies* (Washington, D.C.: Carnegie Institution of Washington with the Flintridge Foundation)
- Schweizer, F., Seitzer, P., Faber, S. M., Burstein, D., Dalle Ore, C. M., & González, J. J. 1990, *ApJ*, 364, L33
- Schweizer, F. & Seitzer, P. 1992, *AJ*, 104, 1039
- Spinrad, H. & Taylor, B. 1971, *ApJS*, 22, 445
- Tantalo, R., Chiosi, C., & Bressan, A. 1998a, *A&A*, 333, 419
- Tantalo, R., Chiosi, C., Bressan, A., Marigo, P., & Portinari, L. 1998b, *A&A*, 335, 823
- Thomas, D., Greggio, L. & Bender, R. 1999, *MNRAS*, 302, 537
- Tinsley, B. M. 1980, *Fund. Cosmic Phys.*, 5, 287
- Trager, S. C. 1997, Ph.D. Thesis, University of California, Santa Cruz
- Trager, S. C., Worthey, G., Faber, S. M., Burstein, D., & González, J. J. 1998, *ApJS*, 116, 1
- Trager, S. C., Faber, S. M., Worthey, G., & Gonzalez, J. J. 2000, *AJ*, 119, 1645 (Paper I)
- Tripicco, M. & Bell, R. A. 1995, *AJ*, 110, 3035 (TB95)
- Vader, J. P. 1986, *ApJ*, 305, 669
- Vader, J. P. 1987, *ApJ*, 317, 128
- van den Bergh, S. & Tammann, G. A. 1991, *ARA&A*, 29, 363
- Vazdekis, A., Casuso, E., Peletier, R. F., & Beckman, J. E. 1996, *ApJS*, 106, 307
- Visvanathan, N. & Sandage, A. 1977, *ApJ*, 216, 214
- Wheeler, J. C. & Harkness, R. P. 1990, *Rep. Prog. Phys.*, 53, 1467
- Woosley, S. E. & Weaver, T. A. 1995, *ApJS*, 101, 181
- Worthey, G. 1992, Ph.D. Thesis, University of California, Santa Cruz
- Worthey, G. 1994, *ApJS*, 95, 107 (W94)
- Worthey, G. 1996, in *From Stars to Galaxies: the Impact of Stellar Physics on Galaxy Evolution*, ed. C. Leitherer, U. Fritze-von-Alvensleben, & J. Huchra, ASP Conf. Ser., vol. 98 (San Francisco: ASP), p. 467
- Worthey, G. 1998, *PASP*, 110, 888
- Worthey, G., Faber, S. M., & González, J. J. 1992, *ApJ*, 398, 69
- Worthey, G., Faber, S. M., González, J. J., & Burstein, D. 1994, *ApJS*, 94, 687
- Worthey, G., Trager, S. C., & Faber, S. M. 1996, in *Fresh Views on Elliptical Galaxies*, ed. A. Buzzoni, A. Renzini, & A. Serrano, A. S. P. Conf. Ser., vol. 86 (San Francisco: ASP), p. 203
- Ziegler, B. L. & Bender, R. 1997, *MNRAS*, 291, 527